Ultrasonics 155 (2025) 107726



Contents lists available at ScienceDirect

Ultrasonics

journal homepage: www.elsevier.com/locate/ultras





On the robustness of coded excitation in ultrasonic acquisition systems

Connor Challinor, Frederic Cegla *

Department of Mechanical Engineering, Imperial College London, Exhibition Road, South Kensington, London, SW7 2AZ, UK

ARTICLE INFO

Keywords:
Coded excitation
Ultrasonics
Acquisition hardware
Non-stationary measurements

ABSTRACT

Coded excitation has been shown to be a simple yet effective technique for improving signal quality in ultrasonic active ranging applications. Despite many reported benefits, uptake of coded excitation in industrial applications to date has been minimal. The authors speculate that this can be in part attributed to a lack of understanding of the robustness of the technique in practical use. To combat this, this paper reports on research into the main mechanisms that can introduce performance degradation and describes the effect of the two most important mechanisms, referred to as symbol asymmetry and symbol misalignment. These mechanisms lower output signal quality through the introduction of unexpected signal artifacts, as well as by reducing useful signal amplitude. We show how symbol asymmetry can be introduced through hardware imperfections and the relative degradation severity associated with different imperfection types. We similarly show how symbol misalignment can be introduced when using coded excitation in non-stationary situations. As a result, we formulate the minimum hardware requirements and inspection conditions required to correctly utilise coded excitation such that users can be confident of achieving high quality outcomes. We quantitatively simulate and experimentally verify the output signal degradation across many scenarios to identify the operating conditions that need to be satisfied to ensure that degradation does not exceed an arbitrarily chosen threshold of 40 dB (the noise floor from random noise in our experimental setup).

1. Introduction

Ultrasonic signal acquisition is an essential tool for industrial Non-Destructive Evaluation (NDE) and medical imaging where it is used for the characterisation of materials, components and structures. Therefore, improving overall system performance (i.e., signal/image quality, acquisition rate, system efficiency, etc.) of ultrasonic acquisition systems is a prominent research topic. In literature, coded excitation is a well documented technique which has been shown to be a simple and effective technique for improving signal acquisition performance [1–18].

Coded excitation is a technique that employs the transmission of temporally long coded sequences which are pulse compressed upon reception to produce high intensity temporally narrow signals. To implement coded sequences as transmission signals, control sequences are used to dictate the start phase of a pulse, called the symbol, such that the transmission signal is made from many symbols back-to-back each with a specific start phase (i.e., a phase modulation is introduced). With coded excitation, the control sequence dictates the compression performance of the introduced modulation, therefore meaning the symbol can be arbitrarily chosen. This allows for the technique to be simple as it requires only bipolar pulsing, something available on most standard acquisition systems.

Despite many publications highlighting the benefits of coded excitation, with some suggesting that the technique could allow for the development of the next generation of portable systems [2,3,17,19,20], the technique has typically remained limited to research applications. To the best of the authors' knowledge, there are currently no commercial systems that employ coded excitations.

The authors speculate that the lack of uptake of coded excitation is partially due to a lack of understanding of the robustness of the technique when used in real applications. Whilst there has been lots of research into the fundamentals of using coded excitation, little work has focused on investigating how the technique behaves when presented with the practical challenges that can be introduced in real life settings. Therefore, in this paper, we investigate the performance degradation that can result from imperfections in ultrasonic measurement systems when using coded excitation.

The structure of the paper is as follows: Section 2 first defines what we mean by performance degradation of coded excitations. Section 3 then introduces the main mechanisms that cause performance degradation. Using both simulations and experiments, Section 4 investigates symbol asymmetry arising from hardware imperfections. Section 5 investigates symbol misalignment due to movement of a non-stationary inspection platform. Finally, conclusions are drawn in Section 6.

* Corresponding author.
E-mail addresses: cjc220@ic.ac.uk (C. Challinor), f.cegla@imperial.ac.uk (F. Cegla).

https://doi.org/10.1016/j.ultras.2025.107726
Received 10 December 2024; Received in revised form 3 April 2025; Accepted 10 June 2025
Available online 24 June 2025
0041-624X/© 2025 The Author(s). Published by Elsevier B.V. This is an open access article under the CC BY license (http://creativecommons.org/licenses/by/4.0/).

2. Defining performance degradation

When using binary sequences to create coded excitations (using a simple process as outlined in more detail in [17]), each sequence element in a coded excitation corresponds to the consecutive transmission of a symbol of either a positive or negative start phase. The symbol here is a predetermined pulse of appropriate bandwidth for the given application/transducer (most simply bipolar square waves). The transmission of multiple symbols results in an improvement in SNR following pulse compression with the SNR gain (against random noise) being proportional to the chosen sequence length (which determines the increase in transmission energy) [1,18,21]. The main factor to consider when designing a coded excitation is selecting a suitable sequence as this determines the signal quality improvements that can be achieved.

An ideal sequence has a perfect autocorrelation function of only a single high-amplitude spike — this enables SNR improvements without introducing complicated filter artifacts. However, with traditional binary sequences (which are the focus of this work), perfect compression is not possible [14]. Instead, autocorrelation of a sequence results in a Main Lobe (ML) at the central lag and a symmetric distribution of Side Lobes (SLs) at all other lags (also shown in [17]). In ultrasonic measurements, this translates into filtered signals containing large echoes for each reflector (the MLs) which are surrounded by a cluster of unwanted artifact echoes (the SLs). The amount of coherent noise introduced by the artifact echoes is determined by the compression performance of the chosen sequence and should be minimised to produce useful measurements.

The compression performance of a sequence can be quantified using its Merit Factor [22]. A sequence's Merit Factor is found by calculating the ratio of the peak ML energy and the total energy contained within all other lobes. A different metric that we will instead use to classify a sequence's compression performance is Peak-to-Side-Lobe-Ratio (PSLR). PSLR compares the peak power in the ML to the peak power in any of the SLs. PSLR is different to the Merit Factor in that it is concerned only with the impact of the largest SL. A sequence can have a high Merit Factor by producing a single large SL, however, it will not be ideally suited to active ranging as a high amplitude SL can be easily mistaken for a ML from a different reflector. This same sequence would instead have a low PSLR, making this second metric more suited for determining the usefulness of a sequence for active ranging applications where multiple low amplitude SLs are more tolerable.

Sequence optimisation options for minimising the impact of SLs do exist. This is through either minimising the peak side lobe amplitude, such as with Barker sequences (i.e., produce many low-amplitude SLs), or through the complete removal of SLs using pseudo-periodicity [17] or sequence pairs such as Complementary Golay Sequences (CGSs) [23–25]. This work will use CGSs as the preferred optimisation step given their greater popularity. With CGSs, the filter response of each part of the complementary pair contains SLs that are alike in position but opposite in amplitude, therefore summing each filter response allows for the SLs to be cancelled out.

Once a sequence option has been selected, the result from using the coded excitation on an ultrasonic measurement can be predicted. The SNR will increase and each reflector will get its own lobe distribution — that is a ML and a symmetric collection of SLs (or SLs will be removed depending on the chosen sequence type). Assuming that the system behaves as expected, the lobe distribution for each reflector will match that of the output from the sequence's autocorrelation. With this assumption, the benefits of the technique become clear — coded excitation is a simple method that can greatly improve signal quality. If SLs are not going to be removed from sequence optimisation, they can at least be accounted for when the system designer knows where they are expected to arrive relative to each ML.

However, should the assumption that lobes will be distributed according to the sequence's autocorrelation no longer hold true, using the technique becomes far more complicated. Should MLs and SLs be redistributed, it will be difficult to determine whether a given lobe in the final signal corresponds to a unique reflector or something else entirely. Therefore, it is important to understand whether the technique is robust in its ability to produce the expected lobe distribution when faced with practical challenges, hence the motivation for this work. We are defining any system imperfection or practical challenge that results in a redistribution of lobe energy as a performance degradation mechanism. In the following section, we introduce the main degradation mechanisms that are relevant to ultrasound inspections.

A final note on defining performance degradation: the following sections investigate how system imperfections can alter PSLR. A second form of performance degradation exists when using sequence orthogonality for simultaneous multi-channel coded excitation measurements, such as shown in [12,13,17]. In these applications, orthogonal sequences achieve ideal (or ideal-like) cancellation when correlated against each other to remove crosstalk from neighbouring channels. The following degradation mechanisms can also alter the ability to achieve ideal orthogonality, however, the severity of this degradation is less than that which occurs with respect to a change in PSLR, therefore the following focuses only on this metric for brevity.

3. Degradation mechanisms

Having explained the motivation for studying degradation mechanisms that can introduce unexpected compression with coded excitations, this section introduces the main degradation mechanisms of interest in ultrasonic applications.

To understand how each degradation mechanism behaves, a full coded excitation filter response is not needed. Instead, sequence autocorrelation functions by themselves can be used. Example 1 shows the ideal autocorrelation of a pair of $L = 4$ CGSs. In the following, autocorrelation is shown as a convolution, $\otimes$, of the sequence against the time reversal of itself, denoted with a left arrow caret.

Example 1. Let $A1 = [-1, -1, +1, -1]$ and
$A2 = [-1, -1, -1, +1]$ and
$R_{A1,A1} = A1 \otimes \overleftarrow{A1}$ then:

$$R_{A1,A1} = [+1, 0, -1, +4, -1, 0, +1]$$
$$R_{A2,A2} = [-1, 0, +1, +4, +1, 0, -1]$$
$$R_{A1,A1} + R_{A2,A2} = [0, 0, 0, +8, 0, 0, 0]$$

The structure of a sequence is, in a way, simple. There are a certain number of elements in a particular order each with a corresponding value (of either +1 or −1 when considering binary sequences). As such, there are only two ways in which the sequence structure can be altered – a change in an element's position or value.

Symbol asymmetry

Starting with changing an element's value, the first main degradation mechanism can be explained. We are calling this *Symbol Asymmetry* and it relates to a redistribution of lobes arising from an element (or many elements) having an incorrect energy. The following examples demonstrate the degradation resulting from symbol asymmetry. In each of the following, the correlation is undertaken against the ideal sequence(s), as would be done when the assumption made is that the ideal response will be returned.

Example 2. Let $B1 = [-1, -1, +1, -0.9]$ and
$B2 = [-1, -1, -1, +1]$ then:

$$R_{B1,A1} = [+1, 0, -1, +3.9, -0.9, -0.1, +0.9]$$
$$R_{B2,A2} = [-1, 0, +1, +4, +1, 0, -1]$$
$$R_{B1,A1} + R_{B2,A2} = [0, 0, 0, +7.9, +0.1, -0.1, -0.1]$$

Example 3. Let $C1 = [-0.9, -0.9, +0.9, -0.9]$ and $C2 = [-0.9, -0.9, -0.9, +0.9]$ then:

$$R_{C1,A1} = [+0.9, 0, -0.9, +3.6, -0.9, 0, +0.9]$$
$$R_{C2,A2} = [-0.9, 0, +0.9, +3.6, +0.9, 0, -0.9]$$
$$R_{C1,A1} + R_{C2,A2} = [0, 0, 0, +7.2, 0, 0, 0]$$

and

$$R_{A1,A1} + R_{C2,A2} = [+0.1, 0, -0.1, +7.6, -0.1, 0, +0.1]$$

Firstly, Example 2 demonstrates how symbol asymmetry introduces a change in the ML and SL amplitudes. When a sequence element is of an incorrect value, the sequence structure is not maintained, therefore the expected ML and SL distribution is not produced following correlation — this is shown by comparing the values of $R_{A1,A1}$ and $R_{B1,A1}$. With CGSs as the example, this further results in non-perfect SL cancellation, therefore reducing PSLR, as well as a general reduction in SNR due to the reduction in ML amplitude.

Example 3 then shows that symbol asymmetry refers only to some sequence elements being of incorrect value relative to each other. When all element values are similarly scaled to the same new value, as would be the case when considering insertion losses resulting in reduced echo amplitudes in an ultrasonic measurement, the sequence structure is still maintained. The only difference in output arising from a uniform change in element amplitude is an altered resulting SNR. One additional point relating specifically to the use of CGSs is that cross-sequence total energy symmetry must be maintained for perfect SL cancellation to be achieved, therefore, CGSs have an additional degradation mechanism to consider compared to alternative sequence types (also shown in Example 3).

Examples 4 and 5 expand further upon symbol asymmetry related performance degradation:

Example 4. Let $D1 = [-1, -1, +1, -0.7]$ and $D2 = [-1, -1, -1, +1]$ then:

$$R_{D1,A1} = [+1, 0, -1, +3.8, -0.8, -0.2, +0.8]$$
$$R_{D2,A2} = [-1, 0, +1, +4, +1, 0, -1]$$
$$R_{D1,A1} + R_{D2,A2} = [0, 0, 0, +7.8, +0.2, -0.2, -0.2]$$

Example 5. Let $E1 = [-1, -0.9, +1, -0.9]$ and $E2 = [-1, -1, -1, +1]$ then:

$$R_{E1,A1} = [+1, -0.1, -0.9, +3.8, -1, -0.1, +0.9]$$
$$R_{E2,A2} = [-1, 0, +1, +4, +1, 0, -1]$$
$$R_{E1,A1} + R_{E2,A2} = [0, -0.1, +0.1, +7.8, 0, -0.1, -0.1]$$

Examples 4 and 5 show that the severity of the performance degradation (i.e., the amount lobes change from their expected amount) is dependent on the total amount of symbol asymmetry. This means that a single large change or many small changes are equally detrimental when considering the total amount of incorrect SL energy that is produced. However, when considering PSLR as the most important metric, a larger number of small symbol asymmetries is preferable to a single larger asymmetry, depending on the order of sequence elements.

Symbol misalignment

The second degradation mechanism then relates to the only other way the sequence structure can be altered — changing the position of an element. This mechanism, which we are calling *Symbol Misalignment*, occurs when a symbol is out of position with respect to the position of the other symbols. This does not relate to symbols swapping position with each other as it is assumed that the correct sequence will always be transmitted at the beginning of a measurement. Instead, this relates to a mechanism resulting in the repositioning of a symbol, i.e., a symbol is returned too early or too late respective of the arrival of the preceding or following symbol. The result of symbol misalignment is shown in Example 6.

Example 6. Let $G1 = [-1, -1, +1, 0, -1]$ and $G2 = [-1, -1, -1, +1, 0]$ then:

$$R_{G1,A1} = [0, +1, 0, -1, +3, +1, -2, +1, +1]$$
$$R_{G2,A2} = [0, -1, 0, +1, +4, +1, 0, -1, 0]$$
$$R_{G1,A1} + R_{G2,A2} = [0, 0, 0, 0, +7, +2, -2, 0, 1]$$

Example 6 shows an extreme symbol misalignment where an element is delayed by a full symbol's width which is not expected to occur in real measurements. However, it illustrates that with severe symbol misalignment, severe performance degradation occurs as a result of a substantial redistribution of lobe energy.

In this section, we have introduced symbol asymmetry and symbol misalignment as performance degradation mechanisms. In the following sections we will discuss how they arise in real life applications: Section 4 focuses on how hardware imperfections can introduce symbol asymmetry; Section 5 then focuses on the introduction of symbol misalignment when employing coded excitations on a non-stationary platform.

4. Hardware challenges

There are multiple ways in which *Symbol Asymmetry* can be introduced during ultrasonic measurements. The most notable is when imperfections are present in the acquisition hardware. Hardware imperfections are of significant concern as, without understanding them, hardware that exploits the benefits of coded excitation cannot be built. This section uses both simulations and experiments to show the severity of performance degradation that can occur when using imperfect acquisition hardware. First, the components of a traditional acquisition system are introduced and how they can result in degradation is covered.

4.1. Traditional acquisition systems

The typical components within a traditional acquisition system are shown in Fig. 1. The sub-systems of interest in terms of introducing performance degradation are: Energy Delivery; Energy Reception; and Transduction. Firstly, we use the transduction sub-system to show only non-linear energy distortions cause significant performance degradation.

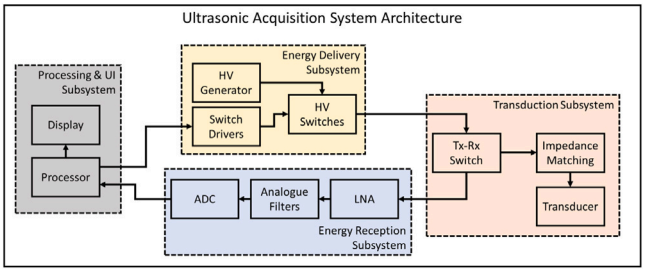


Fig. 1. Traditional components of a single-channel ultrasonic acquisition system broken into key sub-system groups.

The transduction sub-system contains only the ultrasound transducer and the transmit-receive switch (if one is used). Most, if not all, ultrasound transducers have a fixed bandwidth over which they can operate most effectively. We will refer to this bandwidth restriction as the Transducer Transfer Function (TTF). Due to the TTF, most transducers cannot match simple bipolar square wave transmission signals, which are the simplest way coded excitations can be applied. As a result, each symbol in the coded excitation is filtered by the TTF which results in symbol energy distortion. This can produce symbol asymmetry, particularly during symbol phase reversals. However, the transducer distortion acts as a linear function. This means that each symbol can be assumed to receive an equal level of distortion which

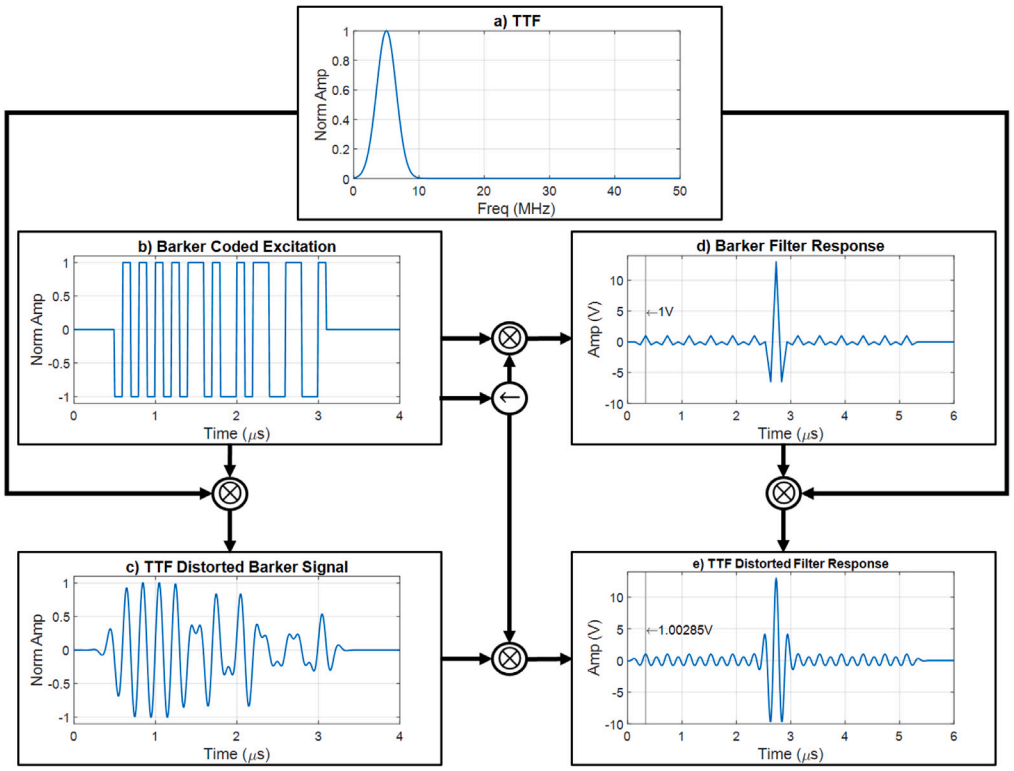


Fig. 2. Compression performance of a coded excitation against both the transmission signal itself and a TTF distorted coded excitation. *(a)* a model TTF using a Gaussian shape with 5 MHz centre frequency and 1.5 MHz standard deviation. *(b)* a Barker coded excitation using a 1-cycle 5 MHz symbol and a code length of $L = 13$. *(c)* the TTF function of *a* applied to the coded excitation of *b*. *(d)* the autocorrelation of the coded excitation of *b* with the peak SL amplitude shown. *(e)* the cross-correlation of the coded excitation in *b* with the TTF distorted signal in *c*, which is equivalent to applying the TTF distortion to the autocorrelation signal from *d*.

will not result in any substantial performance degradation. This is also equivalent to assuming that the TTF does not impact the lobe distribution until after compression has been achieved based on ideal transmission and reception characteristics.

To demonstrate the negligible degradation arising from the introduction of a linear function, Fig. 2 shows the impact of a TTF (TTF parameters of a Gaussian shape with 5 MHz centre frequency and 1.5 MHz standard deviation) when applied to a Barker coded excitation (using a 1-cycle 5 MHz symbol). Following the introduction of the TTF, the PSLR of the Barker filter response remains similar and only the lobe shapes are changed (a minor PSLR change does occur arising from constructive interference from TTF-induced lobe widening). For clarification, should CGSs have been used in Fig. 2, perfect cancellation would still have been achieved.

Having explained that only hardware imperfections that introduce symbol asymmetry via non-linear distortions are of concern, the degradation that can occur from imperfections in the remaining sub-systems can be introduced. Both the energy delivery and reception sub-systems are capable of introducing non-linear symbol distortions through many mechanisms. For the sake of brevity, we focus only on the imperfection mechanisms listed below which we have found to be the most significant in introducing performance degradation, each of which are also shown in the first column of Fig. 3.

- A Rise/Fall Slew Asymmetry – a difference in the time taken to rise to the peak transmission voltage versus falling down to baseline zero volts (or vice-versa)
- A Rail Slew Asymmetry – a difference in the rise and/or fall time of the symbol across the two rails
- A Symbol DC Offset – a difference in the absolute voltage rating of the positive and negative half-cycles

In Fig. 3, $L = 8$ CGS coded excitations are created using symbols that contain the listed imperfection mechanisms. The filter responses for each of the resulting coded excitations are then shown on a log scale (normalised to the peak of the ML). This is repeated with and without the use of symbol zero-padding — the process of adding zero-valued spacing between symbols. Adding symbol spacing results in filter responses that contain an equivalent lobe distribution except for the addition of similar spacing between all SLs. When using zero-padding in Fig. 3, the filter responses are shown for both of the complementary coded excitations as well as the final summed output. Fig. 3 shows that the presence of the imperfection mechanisms all result in a substantial change in PSLR given CGSs expect to achieve complete SL cancellation (as shown in the first row).

Fig. 3 is useful in explaining how symbol asymmetry mechanisms can result in a redistribution of SL energy. With each of the listed mechanisms, the total level of energy asymmetry that results is minor — each symbol has more or less the same total energy as all neighbouring symbols. However, the distribution of energy throughout each symbol is notably different. Taking DC offset as the most simple example, the positive half of the symbol contains more energy than the negative half — the symbol's energy is front loaded for positive phase symbols. The opposite is then true for negative phase symbols. Therefore, the symbol energy distribution for neighbouring symbols is different which alters the equivalent sequence structure. This results in a redistribution of SL energy for expected SLs as well as an introduction of new SLs — this is shown by viewing the filter output from coded excitations that contain symbol zero-padding. With the breakdown mechanisms present, the original ML and SL distribution is more or less maintained in terms of position, but new unique SLs are introduced (which are typically lower amplitude than the expected SLs). Additionally, each

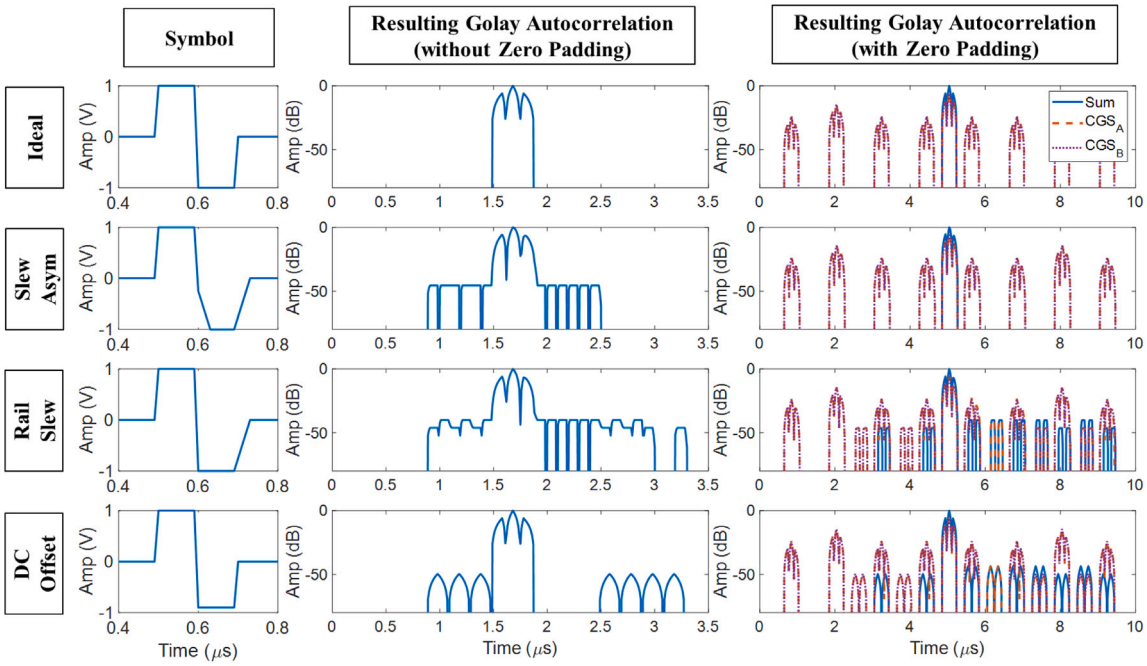


Fig. 3. Symbol asymmetry types that can be introduced by the energy transmission sub-system. The first column shows the change in appearance of a 1-cycle square wave symbol when each of the listed degradation mechanisms are present. The central column shows the resulting filter response when using $L = 8$ CGSs to form coded excitations using each of the symbol types. The final column shows the resulting filter response (of both complementary signals and their sum) when introducing zero-padding between symbols when creating the CGS based coded excitations.

of the expected SLs are modified slightly with respect to their energy distribution. As each sequence structure is altered in a unique way, the change in SL energy that is introduced results in a substantial performance degradation when using CGSs where ideal SL cancellation is expected.

The mechanisms shown in Fig. 3 can be introduced by the energy reception sub-system during receiver amplification and signal digitisation, however, they are much more likely to be produced by the energy delivery sub-system. To produce bipolar square wave excitations, the most common transmission architecture used is typically a half-bridge configuration — as is integrated in many off-the-shelf ultrasound pulser chips such as the MAX14808 [26] and STHV800 [27]. This configuration is rugged, simple and scale-able as it uses just a single PMOS and NMOS MOSFET per channel (PMOS for positive pulses, NMOS for negative). The use of differing MOSFET doping technologies for producing opposing polarity pulses is what can introduce the symbol asymmetry, though, as NMOS and PMOS transistors inherently have differences in their electrical characteristics. This can lead to a difference in rise and fall times and in the absolute voltage rating across the rails, hence how a DC offset or (rail-specific) slew rate asymmetry can be introduced.

To verify that this hardware architecture can result in the listed breakdown mechanisms, a MAX14808 evaluation board was used to produce $L = 16$ CGS coded excitations with a peak amplitude of 30 V. An FPGA evaluation board was interfaced to the pulser evaluation board such that the coded excitations could be produced. The coded excitation signals were then recorded using a Handyscope HS5-540XM (HS5) USB oscilloscope which was set to measure over a ±40 V range with a 14-bit precision and with a sample frequency of 100 MHz. The pulser output was connected to the oscilloscope input with a T-junction and a 50 Ohm load such that the pulser was running under more realistic operating conditions. The resulting excitations and filter response are shown in Fig. 4 in which substantial performance degradation can be seen, as can the presence of imperfections in the excitation signal. The imperfections are further highlighted in row four of Fig. 4 which shows the subtraction of the CGSs from each other — the first half of the CGSs are the same, meaning the first half of the cancellation should be zero.

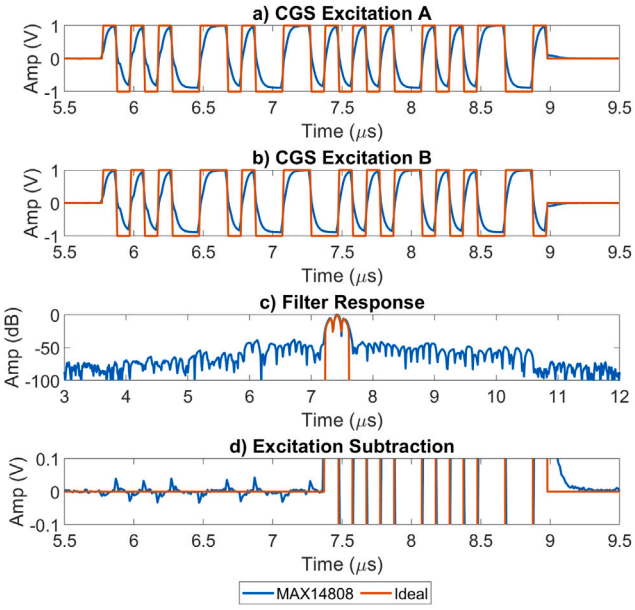


Fig. 4. Performance degradation when using the MAX14808 pulser evaluation board with $L = 16$ CGSs created with a 1-cycle 5 MHz square wave symbol. *(a–b)* Each of the complementary pair of coded excitations. *(c)* The summed filter response. *(d)* The subtraction of the two complementary signals. In each plot, the ideal signal is shown for reference.

For clarity, it is worth stating that we are not implying that ideal rise/fall characteristics are required of the pulser hardware. It is difficult/impossible to produce hardware that can create instantaneous rise and fall edges for square wave excitations. However, imperfections that lead to a decreased slew rate are not of concern as long as the rise and fall characteristics are symmetric. Performance degradation occurs only when symbol asymmetry is present.

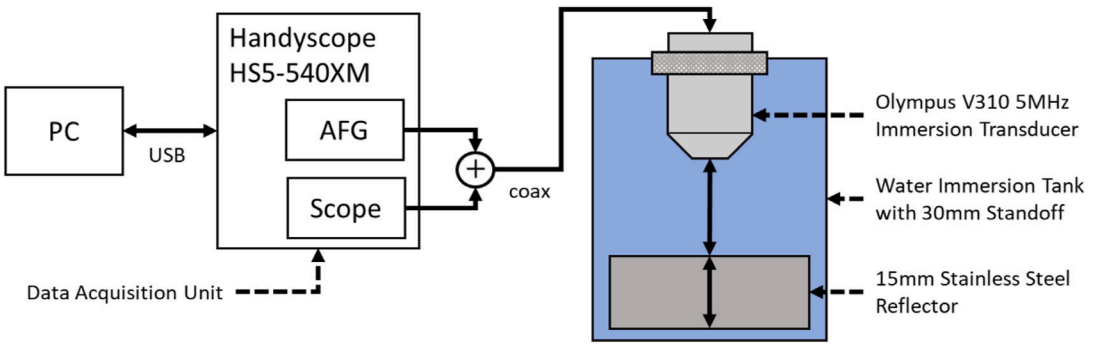


Fig. 5. Immersed transducer pulse-echo application used to investigate the degradation severity with varying hardware imperfection severity. A Handyscope HS5 USB function generator and oscilloscope is used as a complete data acquisition system. An Olympus V310 5 MHz centre frequency immersion transducer is used with a 15 mm stainless steel reflector placed 30 mm from the transducer surface.

Having explained how hardware imperfections can introduce a performance degradation, the following sub-section investigates the severity of performance degradation that occurs for varying degrees of imperfection level for each of the previously listed mechanisms.

4.2. Degradation severity

To investigate the severity of performance degradation as a function of the amount of each imperfection mechanism, the setup in Fig. 5 is used. This setup uses an immersed 5 MHz transducer, an Olympus V310, to record pulse-echo measurements of a 15 mm stainless steel reflector placed 35 mm away from the transducer face with the immersion fluid being room-temperature water.

The pulse-echo setup shown in Fig. 5 was first simulated using a simple time-shift approach. The time-delay and transmission and reflection coefficients were calculated for the front wall entry echo, the first back wall reflection and the second back wall reflection. The simulated signal was then obtained by applying a time-shift in the frequency domain to the excitation signal(s) for each calculated time delay such that three sets of coded echoes were produced — these were then scaled in amplitude using the transmission and reflection coefficients and summed into a single signal. Additionally, the impact of the TTF was included in simulations with TTF parameters of a Gaussian shape with 5 MHz centre frequency and 1.5 MHz standard deviation. The signals were then processed using a full matched filter to produce the final filtered response. Simulations were used such that a very high sample frequency of 500 MHz could be implemented, which allows for fine control when adding in the slew-rate related hardware imperfection mechanisms, and also so that any inherent hardware imperfections and measurement noise that would be present in an experimental platform could be avoided.

In addition to simulations, experiments were performed using an HS5 as both the transmitter and receiver. The HS5's Arbitrary Function Generator (AFG) was used to create and transmit the coded excitations with a sample frequency of 100 MHz and amplitude of ±8 V. The AFG is based on a Digital-to-Analogue Converter (DAC) architecture which allows it to produce excitation signals with a bandwidth of up to 30 MHz without, in theory, any hardware imperfections at this voltage level. In reality, the HS5's AFG will contain imperfections, however, the datasheet of the device [28] states that the AFG can produce signals with an accuracy and symmetry that is sufficient to meet the needs of producing ideal-like coded excitations. The HS5's oscilloscope was then used to record the corresponding echoes over a ±0.4 V acquisition range with 14-bit precision and with the same sample frequency of 100 MHz — no receiver amplification was used. The HS5 operating with these characteristics is able to produce CGS coded excitations that result in no SLs above the measurement noise floor following matched filtering – i.e., the HS5 setup can be considered ideal and is suitable to be used to validate the simulation results. To account for the lack of receiver amplification and to reduce the baseline measurement noise floor, $N = 10$ averaging was used when recording the experimental signals in this section to give an approximately 10 dB SNR gain.

To characterise the performance degradation severity with respect to the severity of the hardware imperfection, the simulation and experimental platforms were used with excitation signals that contained increasing levels of hardware imperfection for each of the investigated imperfection mechanisms. The front-wall echo PSLR for the resultant filtered signals was then recorded by using the peak echo value and the peak value in two 5 μs regions immediately preceding and following the same echo — where any newly introduced SLs would exist. For the experimental platform, this process was repeated 5 times with the average PSLR then taken to mitigate for the impact of random noise spikes. This process was repeated twice, firstly with coded excitations using CGSs of length $L = 16$ and a 1-cycle 5 MHz square wave symbol, and secondly with the same CGSs but with a 2-cycle 5 MHz square wave symbol. The simulation and experimental results are shown in Fig. 6.

For the sake of brevity, the following results focus only on how the hardware imperfections impact PSLR. All of the investigated hardware imperfections also produce a reduction in SNR as they result in a reduction in total transmitted energy. Similarly, all of the investigated imperfections change the bandwidth of the transmission signal which also reduces SNR given the impact of the TTF. A reduction in SNR is a negative consequence of hardware imperfections with coded excitations; however, using coded excitation is still going to produce a higher SNR signal than an uncoded excitation, hence the following focuses only on the specific problem of performance degradation arising from a change in PSLR. For reference, the greatest drop in ML amplitude measured in the following was less than 4 dB (resulting from the largest investigated rail slew rate asymmetry) – this is minor when considering the coded excitations should introduce an SNR gain of approximately 15 dB over a similar uncoded measurement.

In Fig. 6, the x-axis represents the level of imperfection severity. For slew rate related imperfections, each increment corresponds to a 2 ns increase in the respective imperfection (2 ns slower fall time than rise time or 2 ns slower fall time for the negative rail only). For the DC offset imperfection, each step corresponds to a 2% reduction in absolute amplitude for the negative rail.

Firstly, the results in Fig. 6 show a strong match between simulation and experimental results, albeit with the experimental platform having a limit at which PSLR can be measured due to the system noise floor — at roughly 42 dB in Fig. 6-(a) and roughly 48 dB in Fig. 6-(b). This is useful in identifying a threshold at which performance degradation is of concern — a simulated reduction in PSLR that results in SLs below the measurement noise floor is not going to impact overall signal quality. The results further show a strong link between the amount of PSLR related performance degradation and the amount of imperfection level for each mechanism — as is to be expected.

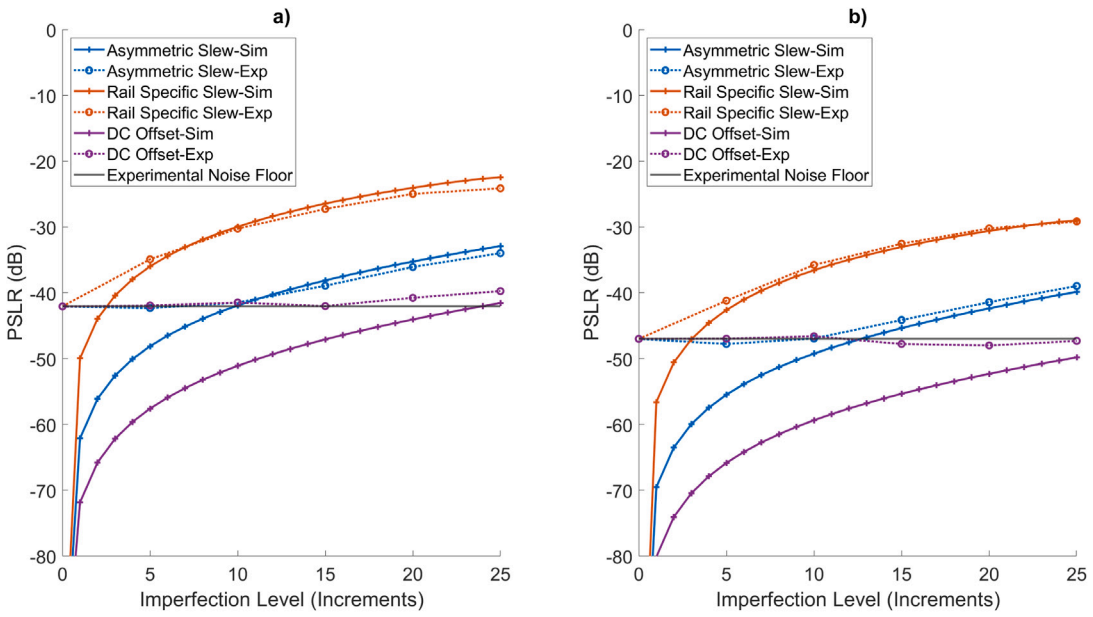


Fig. 6. Degradation severity with increasing imperfection level when using a 1-cycle symbol (a) and a 2-cycle symbol (b) with $L = 16$ CGSs. Imperfection level is presented in increments where each increment corresponds to an increase in the slew rate asymmetry of 2 ns or an increase in rail amplitude asymmetry of 2%.

Secondly, the results show that for slew asymmetry and DC offset imperfections, performance degradation is minor. It takes until at least 20 ns of slew asymmetry before the resulting breakdown SLs are measurable above the experimental noise floor. Further increasing the imperfection level to the maximum tested results in a PSLR of roughly 33 dB which the authors are considering tolerable given the SLs sit below the amplitude of the back-wall reverberations. For a DC offset, PSLR did not significantly cross the experimental noise floor for all tested imperfection levels.

Conversely, for rail specific slew rate asymmetry, the performance degradation is substantial. With just a 6 ns difference in the fall time of the negative and positive rails, SLs are introduced above the noise floor. Further increasing the imperfection level results in SLs as large as 20 dB relative to the front wall echo — this is demonstrated in Fig. 7 in which experimental signals are shown for $L = 16$ CGSs with a 1-cycle 5 MHz square wave symbol both with and without a rail specific slew rate asymmetry of 25 increments. The degradation SLs shown in Fig. 7-(h) have an amplitude that almost matches that of the peak of the first back wall reverberation. This highlights how a significantly degraded PSLR can reduce signal quality by making it difficult to clearly distinguish between breakdown artifacts and real echoes, as well as making it difficult to look for information from low amplitude reflectors. The greater degradation associated with rail specific slew rate asymmetry can be explained given this imperfection mechanism results in the greatest asymmetry in energy distribution between positive and negative starting symbols.

Finally, the second column in Fig. 6 highlights that using an increased symbol duration – a multi-cycle symbol – results in a reduction in the performance degradation for all of the investigated imperfection mechanisms. This is logical as a multi-cycle symbol results in all symbols containing each of the imperfection mechanism to a greater extent — i.e., having 2 amplitude switches in each symbol means all symbols contain more slew rate related imperfections. Therefore, the overall symbol asymmetry is reduced, hence the PSLR performance degradation is reduced.

Having demonstrated the relationship between PSLR degradation and imperfection level, the second investigation undertaken in this section was to perform repeat measurements with increasing sequence lengths such that the impact of sequence length on performance degradation could be shown. This investigation was undertaken by using the same simulation and experimental platform as before and providing them with excitation signals of increasing sequence length all with the same level of each imperfection mechanism. The imperfection level was set as 20 increments (40 ns slew rate symmetry, 40% DC offset) and the sequence lengths were increased from $L = 8$ to $L = 128$ in power of 2 increments for a 1-cycle symbol, and from $L = 4$ to $L = 64$ for a 2-cycle symbol (the max sequence length was dictated by the arrival time of the front wall echo). The results from this are shown in Fig. 8.

The results in Fig. 8 show that the PSLR degradation severity can be reduced by increasing the coded excitation sequence length. This is shown by both experimental and simulation results, albeit with experimental results being unable to track the reduction in PSLR from increasing the sequence length when considering slew and DC offset imperfections due to the experimental noise floor limiting the minimum PSLR that could be measured. The reduction in degradation severity that arises from increasing sequence length can be explained by considering that individual longer sequences typically have a better PSLR to begin with; therefore meaning imperfection mechanisms cannot produce as substantial of a change given the mechanisms most significantly provide a performance degradation by changing the amplitude of existing SLs. If the existing SLs are lower in amplitude, changing them by a given percentage will result in a less significant overall change to PSLR.

A final note, there are multiple pairs of CGSs for a given sequence length. Therefore, there are multiple pairs of CGSs based coded excitations with the same energy but with a different sequence structure. For the sake of brevity, we have not shown multiple sets of PSLR results for equivalent length CGSs but with a differing sequence structure. This is because we have found that changing a sequence structure but sticking with a similar sequence length results in very minor changes to the resulting PSLR degradation that can occur – of the order of 1–3 dB – and therefore has minimal overall impact, unlike when changing sequence length itself.

4.3. Discussion of hardware imperfection results

The results presented in this section are useful in aiding system designers understand how to make acquisition systems most effectively use coded excitations.

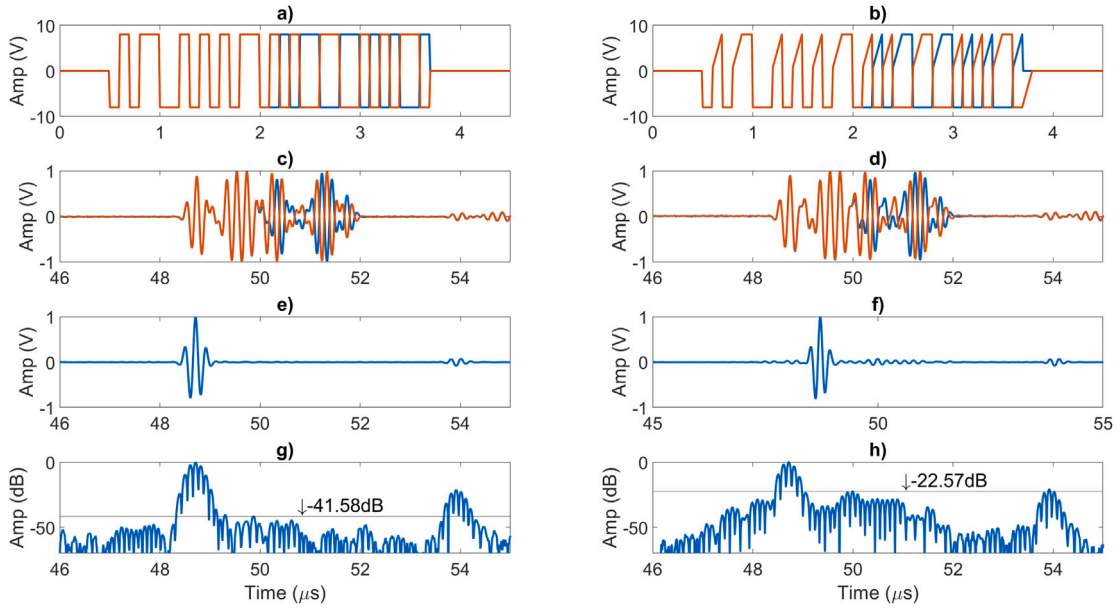


Fig. 7. Difference in appearance of signals with and without the presence of a hardware imperfection. *(a–b)* $L = 16$ CGSs coded excitations using 1-cycle 5 MHz square wave symbols with and without the introduction of 50 ns rail specific slew rate asymmetry. *(c–d)* Corresponding echoes recorded using the excitation signals in *a–b*. *(e–f)* Filtered output from the recorded signals in *c–d*. *(g–h)* Filtered output from the recorded signals in *c–d* shown on a log scale with the position and amplitude of the peak value in the SL measurement region indicated.

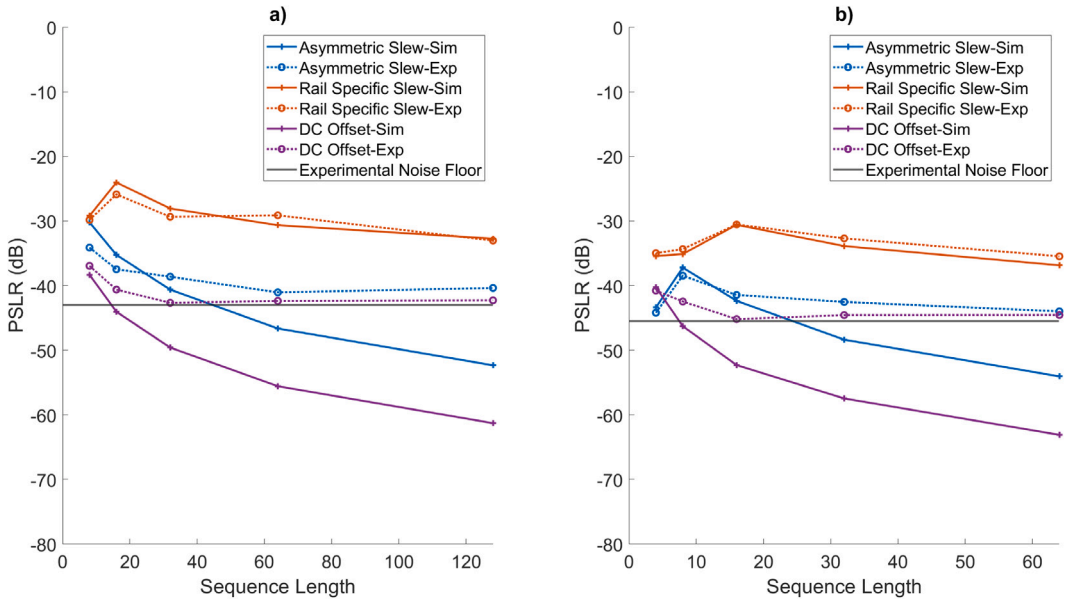


Fig. 8. Degradation severity with increasing sequence length when using a 1-cycle symbol (a) and a 2-cycle symbol (b) with CGSs. The imperfection level for each degradation mechanism is set at 20 increments (40 ns slew rate symmetry, 40% DC offset).

Firstly, the results showed that rail specific slew rate asymmetry is the most significant imperfection mechanism when it comes to altering PSLR. Therefore, system designers can look to use alternative pulsing technologies to avoid the rail specific slew rate asymmetries that are known to exist in half-bridge architectures. Technologies that utilise similar electrical characteristics for positive and negative pulses can be developed, or differential excitations (using only positive/negative pulses applied to opposing sides of the transducer) can be employed to reduce the hardware requirements.

Secondly, the results have shown that longer coded excitations that employ multi-cycle symbols are much more robust against the investigated hardware imperfections. Therefore, system designers can aim to make use of such coded excitation parameters to avoid the need for producing acquisition electronics to stricter requirements. One such technique that could be used is to use the acquisition architecture with TOP-CS sequences introduced in [17], in combination with two-cycle symbols. The setup shown in [17] uses sequence lengths in the thousands which can allow for lower quality electronics to produce PSLR degradation that exists below the noise floor.

Overall, the results shown in this section have highlighted that hardware imperfections can result in a performance degradation, and therefore system designers must be aware of these imperfections. Nonetheless, the results have also shown that, with the exception of rail specific slew rate asymmetry, coded excitation is a robust technique when faced with hardware imperfections as the resulting performance degradation will often sit below the measurement noise floor, especially when longer sequences and symbols are chosen. For applications with a high baseline noise floor of ≤10 dB, even short Barker sequences can be used with significant hardware imperfections to improve overall SNR without introducing any signal quality issues from a drop in PSLR.

Finally, using CGSs to produce the results shown in this section amplifies the apparent level of performance degradation given CGSs expect to achieve ideal SL cancellation. Using sequences with worse compression properties, such as Barker sequences, would have resulted in a negligible change to PSLR as a result of introducing hardware imperfections given such sequences already have a poor PSLR to begin with. For reference, introducing 20 ns of rail specific slew asymmetry to a measurement using $L = 13$ Barker sequences results in a change of PSLR of approximately just 2 dB (from −22.2 dB in the ideal scenario to −20.03 dB).

4.4. Imperfection build-up

Before concluding the hardware section of this work, a final point to address relates to hardware imperfection build-up. That is when multiple hardware imperfection mechanisms are present simultaneously. The previous results investigated each imperfection mechanism in isolation, in reality all of the imperfection mechanisms are likely to exist to some degree at the same time — as shown in Fig. 4.

To investigate imperfection build-up, the same simulation and experimental platform was used. These platforms were provided with coded excitations, all using $L = 16$ CGSs with a 1-cycle 5 MHz symbol, with increasing hardware imperfection levels for one mechanism whilst containing a baseline imperfection level for another mechanism. This was repeated for an increasing DC offset with a baseline imperfection of 15 increments worth of rail specific slew asymmetry and vice versa. The results of this are shown in Fig. 9.

Fig. 9 shows that the system designer should be concerned only with the most significant hardware imperfection mechanism that is present. A baseline imperfection of 30 ns of rail specific slew asymmetry results in a PSLR of approximately 26 dB. Adding up to 50% DC offset increases this only to a PSLR of approximately 24 dB — an insignificant change. Conversely, a 30% DC offset results in a PSLR of 47 dB — adding just 10 ns of rail specific slew asymmetry increases this up to 37 dB which is only 1 dB worse than 10 ns of asymmetry without any DC offset present. This arises as each hardware imperfection mechanism produces its own unique cluster of SLs meaning that the imperfection mechanisms do not ‘work together’ to produce a greater overall performance degradation when multiple mechanisms are present.

5. Motion challenges

The second degradation mechanism investigated in this work is *Symbol Misalignment*. This mechanism occurs when symbols are placed out of position with respect to each other. Assuming the acquisition hardware is correctly programmed, the only way in which a symbol can be out of position compared to its neighbour is if a physical phenomena has resulted in the echo arriving too early or too late. This can occur when coded excitations are used to perform measurements on a non-stationary/moving platform. This section explores the arising performance degradation in this scenario via two sub-investigations, one looking at (vertical) motion of a transducer towards a reflector (Section 5.1), and one looking at (lateral) motion of a transducer across a reflector (Section 5.2). Following these sub-investigations, an industrial application that experiences both motion orientations is introduced and experimental results are shown (Section 5.3).

5.1. Motion towards a target

In NDE applications, motion of a transducer towards a reflector is rare. However, in medical imaging and flow measurement applications, motion towards a target can occur frequently. For example, in medical imaging applications, the inspected material is live tissue which will inevitably be in motion due to patient movement such as breathing. A change in the propagation characteristics due to this type of motion results in a change in arrival time for each of the echoes in the coded measurement, introducing symbol misalignment and the potential for performance degradation.

To investigate the impact of motion towards a target on PSLR, a simple time-dependent simulation was developed. As coded excitations are a collection of back-to-back symbols, simulating a coded excitation propagating through a non-stationary medium can be achieved by simulating each symbol within the signal independently with its own propagation characteristics (propagation distance, speed of sound etc.). By changing the distance to a reflector for each symbol, a collection of echoes can be produced that have ‘experienced’ motion — the latter symbols can utilise a longer/shorter propagation distance to mimic motion of the transducer away from/towards the reflector surface. Summing each simulated echo together allows for the coded echoes to be reconstructed — this signal can then be processed and PSLR can be measured. Taking the case of an immersed pulse-echo measurement of a metal reflector (for simplicity), this simulation methodology is outlined in Fig. 10.

In addition to the simulation methodology of Fig. 10, an experimental setup was used to investigate the degradation severity due to motion towards a reflector. This setup used the same acquisition components as shown in the previous section (Fig. 5) albeit without using averaging (averaging only being possible in stationary systems) and with a larger 5 MHz immersion transducer (Krautkramer, 1 inch diameter). The transducer was placed inside a motorised C-scan tank, as used in [29,30]. This C-scan tank allows for the transducer to be repositioned whilst the HS5 is active, thereby enabling motion of varying velocity (up to 100 mm/s).

To record experimental data, the scanning frame was set to move the transducer away from the reflector from a starting position of 25 mm standoff up to a maximum distance of 50 mm with varying velocities — the transducer was then returned to the original starting position with the same velocity. The HS5 was set to continuously record coded excitation measurements throughout this movement towards and away from the reflector. In post-processing, all signals that were recorded with a front wall standoff between 35 mm and 40 mm were then used to measure the PSLR in the region preceding and following the front wall entry echo — this was done to eliminate measurements taken during the acceleration/deceleration period of the transducer motion. To mitigate the impact of random noise, an average PSLR from 10 measurements within this standoff region was taken.

Both the simulation and experimental signals were used to measure the change in PSLR as the motion velocity towards the target increased. For simulations, this was repeated for velocities up to 500 mm/s in 10 mm/s increments — transducer motion away from the reflector was set to be continuous throughout the entire measurement. For experiments, this was repeated for 10 mm/s, 20 mm/s, 50 mm/s and 100 mm/s velocities. Both simulations and experiments were repeated with varying length CGSs of $L = 16$, $L = 32$ and $L = 64$. As CGSs were chosen, two subsequent measurements were required to produce a final filtered result. This allows for a cross-sequence misalignment to occur due to the time interval between recording (and simulating) each of the complementary pair. To minimise the impact of this time-interval given continuous motion is being investigated, the interval was set as short as possible without resulting in complementary echo overlap — an interval of 150 μs was sufficient to achieve this. The results from both simulations and experiments are shown in Fig. 11.

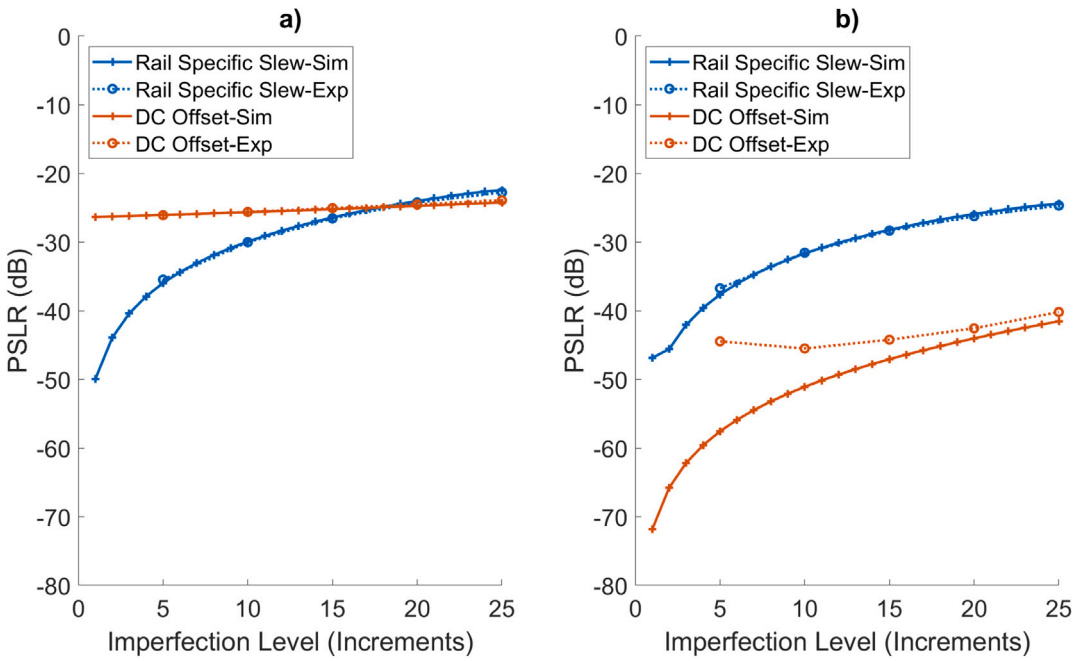


Fig. 9. Degradation severity with increasing imperfection level when using a baseline rail specific slew rate asymmetry (a) and a baseline DC offset (b) and $L = 16$ CGSs. Imperfection level is presented in increments where each increment corresponds to an increase in the slew rate asymmetry of 2 ns or an increase in rail amplitude asymmetry of 2%. Baseline imperfection levels are set at 15 increments (30 ns slew asymmetry, 30% DC offset). Results shown in each plot for the degradation trend introduced by the corresponding baseline mechanism for additional reference.

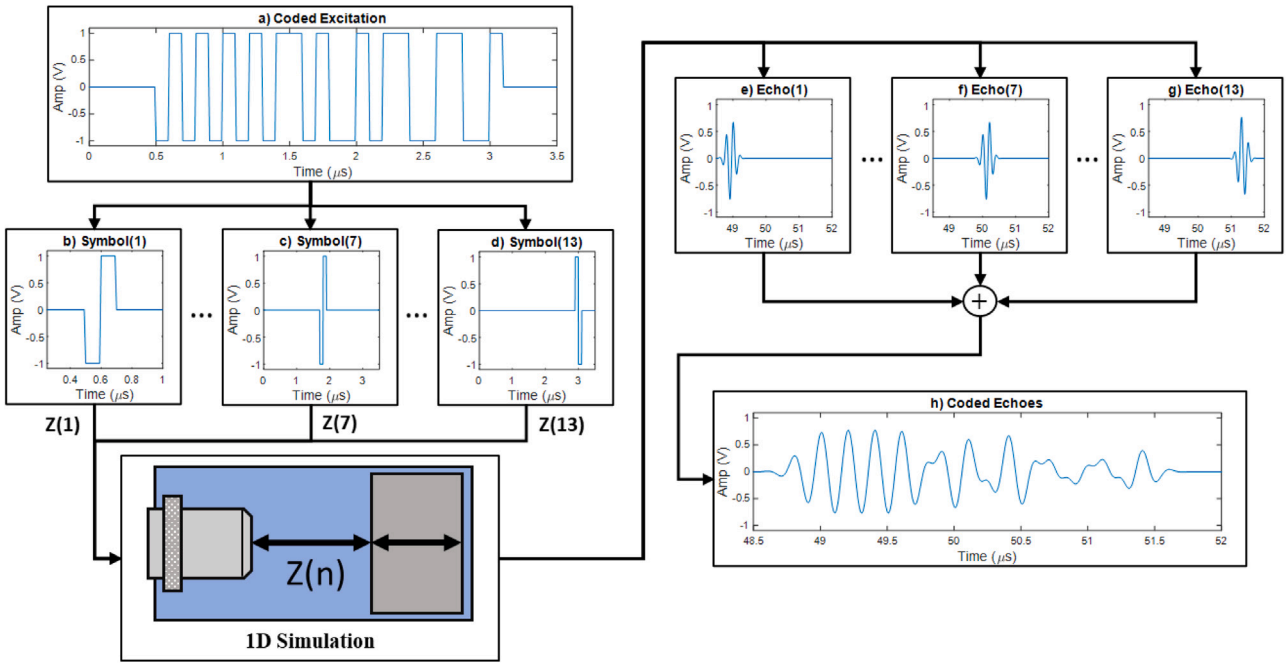


Fig. 10. Simulation methodology for introducing vertical motion into coded excitation measurements. Coded excitations are compartmentalised into their composite symbols which are then individually simulated using a standard 1D approach. The resulting echoes are summed together to produce the resulting coded excitation measurement. Each symbol can be simulated with individualised propagation characteristics (such as standoff distance, denoted with Z(n) in the figure) which allows for motion to mimicked.

The results in Fig. 11 show a substantial PSLR performance degradation as vertical motion velocity was increased — this is shown by both simulation and experimental results which strongly agree. The experimental setup had a noise floor of approximately 40 dB — SLs greater than this level were introduced with just 10 mm/s sustained motion throughout the measurement. However, upon inspection of the recorded signals, it became obvious that the most significant aspect impacting the PSLR degradation was the inter-shot gap between each half of the CGS causing cross-sequence misalignment. With CGSs, ideal SL cancellation can only occur if all lobes are appropriately aligned with their complement across the pair of measurements. The 150 μs inter-shot separation was sufficient to introduce substantial lobe misalignment under these motion scenarios meaning SL cancellation was not being achieved. To correct for this, the simulations and experiments were re-run with an additional processing step included. This additional step was to align the front-wall ML of each of the complementary

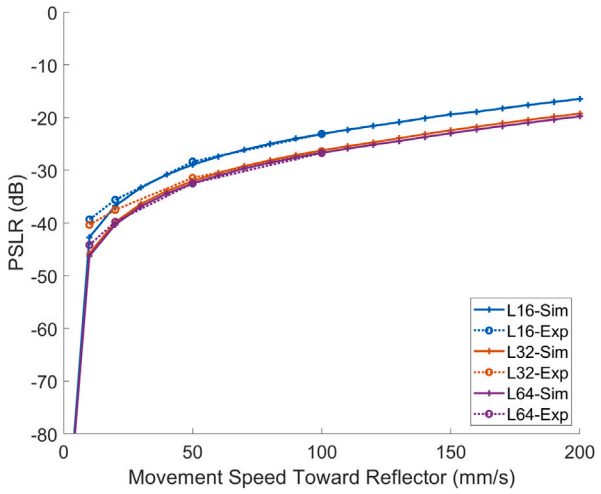


Fig. 11. Degradation in PSLR as vertical motion velocity increases when using CGS based coded excitations of increasing sequence length. A 1-cycle 5 MHz square wave symbol used for all measurements. Both simulation and experimental results presented.

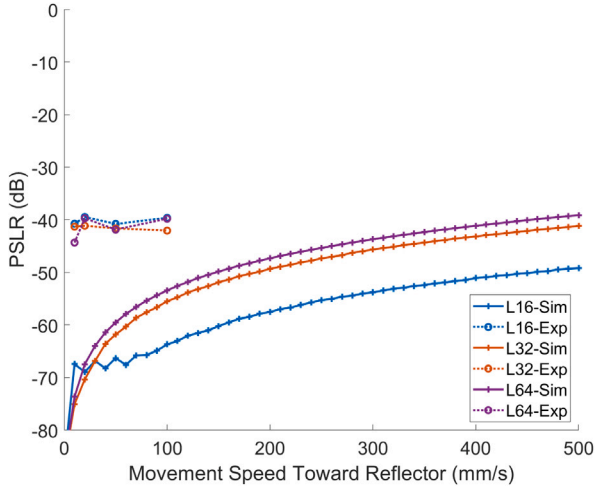


Fig. 12. Degradation in PSLR as vertical motion velocity increases when using CGS based coded excitations of increasing sequence length. A 1-cycle 5 MHz square wave symbol used for all measurements. Both simulation and experimental results presented. For all measurements, ML peak alignment was undertaken during post-processing to eliminate the impact of cross-sequence misalignment.

pair (following signal up-sampling) such that PSLR degradation relating only to inter-sequence misalignment remained. The results from this second round of measurements are shown in Fig. 12.

The results in Fig. 12 instead show that PSLR degradation above the noise floor could not be introduced on the experimental platform given the relatively low top-speed of the C-scan frame. Simulation results do show that PSLR degradation of significant enough magnitude to surpass this noise floor can be introduced, but this does not occur until >450 mm/s sustained motion depending on the chosen sequence length. Increasing the maximum speed investigated using simulations to 2 m/s results in a worst-case PSLR of 27.1 dB (when using $L = 64$ sequences).

The results shown in this section present interesting findings. Firstly, CGS based coded excitations used without ML peak alignment are incredibly susceptible to significant performance degradation due to motion towards a target. Therefore, we strongly recommend that ML alignment should be used in any application where this motion can be encountered. Secondly, even when using peak alignment, coded excitations can suffer a PSLR performance degradation due to intra-sequence vertical motion that can introduce artifacts above the measurement noise floor.

Finally, the results show that performance degradation does not simply reduce when increasing sequence length, unlike the results shown in Section 4. It would be expected that increasing sequence length results in a better PSLR; however, with system motion, an important factor that dictates how much degradation will occur is the total excitation duration. A longer coded excitation can experience a greater total intra-sequence change in propagation characteristics — the first and last symbol can be more greatly misaligned. Therefore, the relative degradation can be more substantial even though the PSLR starting point from using a longer sequence is greater, thus making shorter sequences preferable. This is further highlighted in Fig. 13 in which a collection of signals are shown as the transducer moved away from the reflector. The first row of signals shows measurements from using $L = 16$ 2-cycle CGSs — a total excitation duration (per shot) of roughly 7 μs which resulted in negligible degradation (following peak alignment). The second row of signals shows measurements from using $L = 2000$ TOP-CS coded excitations (which rely on longer sequence lengths to achieve ideal compression [17]) — a total excitation duration of roughly 800 μs which led to a poor worst-case PSLR of −22 dB.

Overall, these results are useful in aiding the system designer to understand how to use coded excitations on a platform that is set to experience motion towards or away from the target. Depending on the motion velocity, performance degradation arising from symbol misalignment is possible. To ensure this sits below the measurement noise floor, the system designer should utilise shorter coded excitations – to minimise first-to-last symbol misalignment – and should similarly use shorter symbols for the same reason. This goes against the recommendations for mitigating hardware imperfections, therefore making the requirements for correctly implementing coded excitations application specific. Furthermore, if using multi-shot sequences (i.e., CGSs or larger complementary families such as those shown in [13]), ML peak alignment should be used to remove cross-sequence misalignment. Nonetheless, overall degradation severity with motion towards a target is low when considering realistic sustained motion velocities (≤1 m/s) and when using short, traditional sequences.

5.2. Motion across a target

In this section, we are now considering the impact of motion of a transducer parallel to primary material boundaries in the inspected medium – i.e., motion across a reflector surface. This scenario is much more common in NDE applications where B-scans and C-scans are regularly produced for mapping material conditions such as corrosion. This orientation is also still common in medical imaging and flow measurement applications.

In contrast to the motion towards a target scenario, when a transducer moves laterally across a reflector, the material's propagation characteristics can remain similar across all symbols if the reflector is homogeneous and defect free. In an immersion application, the couplant thickness can be assumed to remain constant whilst the transducer moves laterally. Therefore, assuming no change in the material properties in the reflector, the propagation characteristics for each symbol are effectively identical despite being in a different position in space. However, in non-immersion applications, such as when using contact transducers or pumped water columns, lateral motion can result in a change in propagation characteristics due to a change in couplant conditions, even if the reflector properties are continuous. Furthermore, if the reflector properties are not continuous, such as due to the presence of a defect, lateral motion will again change the propagation characteristics on a symbol-by-symbol basis which can introduce symbol misalignment. Therefore, the impact of this movement orientation on PSLR must also be studied.

To investigate the impact of lateral motion, both simulations and experiments are once again used. However, the simulation method outlined in Fig. 10 had to be adapted to be able to include lateral motion.

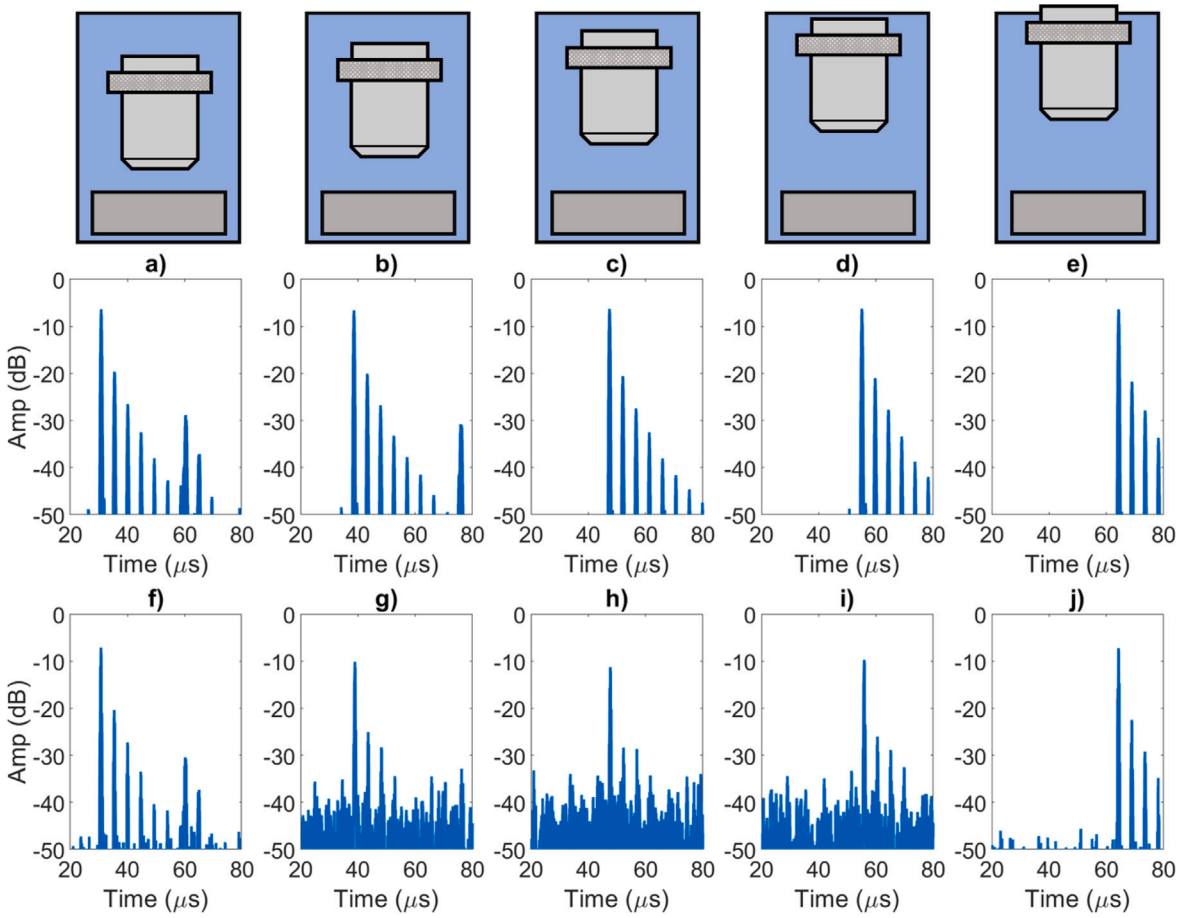


Fig. 13. Signals recorded using the C-scan experimental platform with $L = 32$ CGS coded excitations (*a–e*) and $L = 2000$ TOP-CS code excitations (*f-j*), both with a 2-cycle 5 MHz square wave symbol. All signals shown on a log scale normalised to 100 mV (for CGSs) or 4.5 mV (for TOP-CS). The C-scan was set to vertically move the transducer at 100 mm/s away from the reflector.

Instead of a simple 1D simulation for each symbol, each symbol must be simulated with its own propagation characteristics that encompasses not just the material and couplant thicknesses but also the presence of a scatterer/object/defect within the illuminated area. In this way, each symbol in a coded excitation can be individually simulated such that a full coded result can be reconstructed, and each symbol can account for the transducer emitting over a specific area which can have defects within it. To implement such a simulation methodology, the approach illustrated in Fig. 14 was used. A 2D simulation is approximated as a simple addition of multiple 1D simulations at discrete points over the transducer face. Each 1D simulation is given individualised material properties such that defects can be introduced. Whilst this approach is not as accurate as a more complex model, such as finite element modelling, it is assumed to be sufficient as long as the number of lines per transducer is sufficiently large. For all of the following simulations, the transducer was split into $20 \times (D/\lambda)$ lines where λ is the ultrasonic wavelength in the couplant and D is the transducer diameter (i.e., 20 lines per wavelength). This still allowed relatively fast computation compared to using the finite element method.

The model was then used to measure the PSLR as lateral motion of increasing velocity was introduced. The baseline simulation parameters were set as a 5 MHz immersed transducer (of 6 mm diameter) placed 20 mm away from a 15 mm stainless steel block which is being inspected using L = 8-128 CGS based coded excitations, all with a 1-cycle square wave symbol. This application was simulated with lateral motion ranging from 10 mm/s to 10 m/s across 20 evenly spaced increments. For each simulation, a 10 wavelengths stepped defect was introduced into the front wall after half of the first sequence was transmitted – i.e., the couplant distance increased by 10 wavelengths after the first half of the symbols (in the first of the complementary pair) were transmitted. A stepped defect was chosen as it is the worst case scenario, and the defect was placed in the front wall to give the most significant amplitude SLs. Following post-processing, the PSLR in the region immediately preceding the front wall entry echo was recorded. The results from this are shown in Fig. 15 and example signals from the simulation platform with and without motion are shown in Fig. 16.

In addition to the speed-dependency investigation, the 2D simulation was further used to investigate degradation severity with increasing defect sizes at a fixed lateral motion velocity. For this, the baseline parameters were kept the same and a constant lateral motion of 5 m/s was set. The depth of the stepped defect in the front wall was then increased from 0.25 to 10 wavelengths (in 0.25 wavelength steps) with all defects being introduced halfway through the first set of symbols. The results from this are shown in Fig. 17.

Firstly, Fig. 16 highlights why only the region preceding the front wall entry echo was used to calculate PSLR. The lateral motion of the transducer face across the stepped wall-loss defect results in the majority of the symbols returning with two independent echoes. Therefore, a second ML and cluster of SLs were produced corresponding to this stepped defect. The use of a stepped wall-loss defect in the front wall means that the new lobes follow the original front wall entry echo. To mitigate for the impact of interference between this new lobe distribution and the SLs resulting from imperfect compression, only the region preceding the front wall ML was chosen to measure PSLR.

Secondly, Fig. 15 verifies that, according to this simulation, PSLR reduces as a result of lateral motion across a defect. However, the

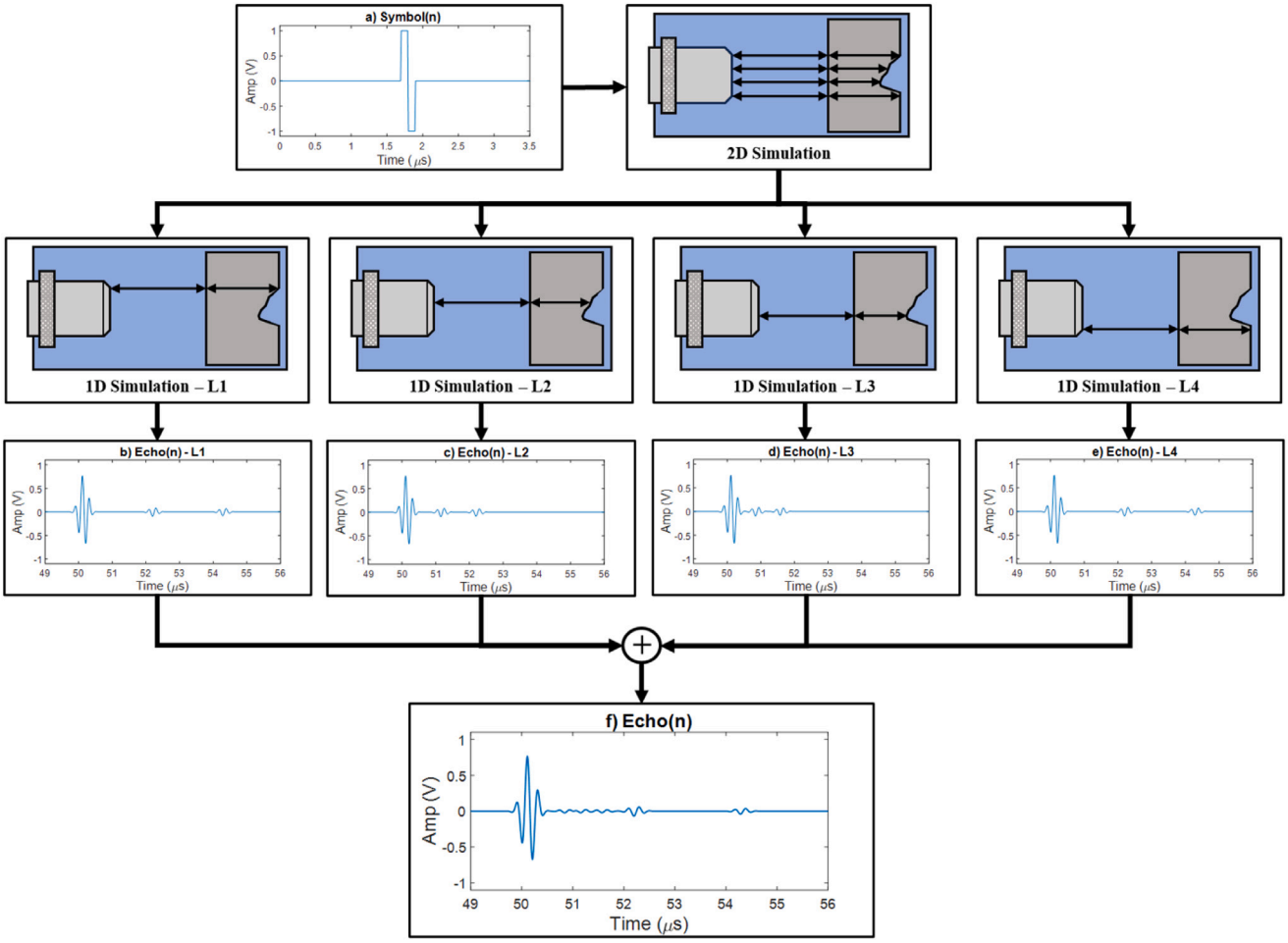


Fig. 14. Simulation methodology for introducing lateral motion into coded excitation measurements. Coded excitations are compartmentalised into their composite symbols which are then individually simulated using a 2D approach — the separation of a coded excitation into composite symbols is shown in Fig. 10. The 2D simulation is itself split into a collection of 1D simulations each with their own respective propagation characteristics. The 2D echo is then reproduced by summing the output of each 1D sub-simulation, and the full set of coded echoes are constructed by repeating the process for all composite symbols and summing the outputs together.

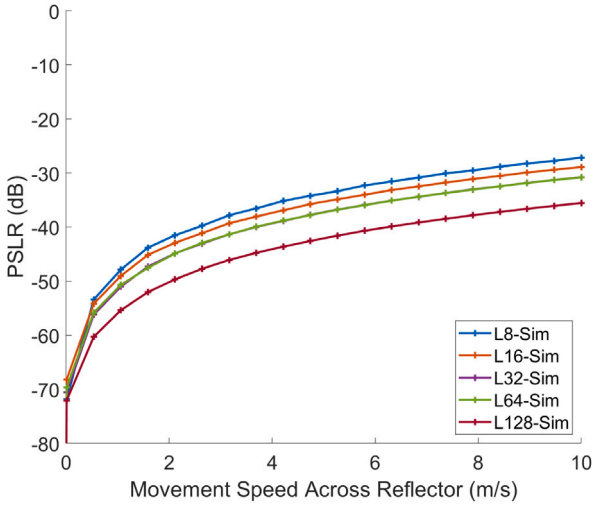


Fig. 15. Degradation in PSLR as lateral motion velocity across a 10 wavelength stepped defect increases when using CGS based coded excitations of increasing sequence length. A 1-cycle 5 MHz square wave symbol used for all measurements. Results obtained using the simulation methodology outlined in Figs. 10 and 14.

change in PSLR is substantially smaller than that corresponding to vertical motion. Over 3 m/s sustained motion is required before PSLR reduces to below −40 dB, the hardware noise floor from these experiments. The reason for this is as follows: with lateral motion, complete symbol misalignment does not occur. Instead, the energy and position of returned echoes varies depending on how much of the defect is illuminated by the transducer face for each symbol. As the defect takes up an increasing amount of the transducer area, the echo energy returned corresponding to the non-defective wall thickness reduces. This energy is then re-positioned to arrive corresponding to the defective wall thickness. Even with substantial motion velocities, the change in inspected area on a symbol-to-symbol basis is minor (symbols are only 200 ns apart in this setup). There is enough re-positioning of energy to create a new low-amplitude ML and SL distribution, but not enough to significantly impact the compression performance compared to the complete misalignment of a symbol, as occurs with vertical motion.

Thirdly, Fig. 17 shows that the severity of performance degradation is not significantly impacted by the size of the defect encountered. This is explained by considering what changing the size of the defect does to the returned symbols. As the defect depth increases, the amount of energy lost that relates to the non-defective thickness does not change, all that changes is where the energy is re-positioned to.

Finally, the results in Figs. 15 and 16 show that the degradation severity is reduced when using longer sequences. With motion towards a target, a longer sequence allows for a greater first-to-last symbol misalignment which can introduce more substantial performance

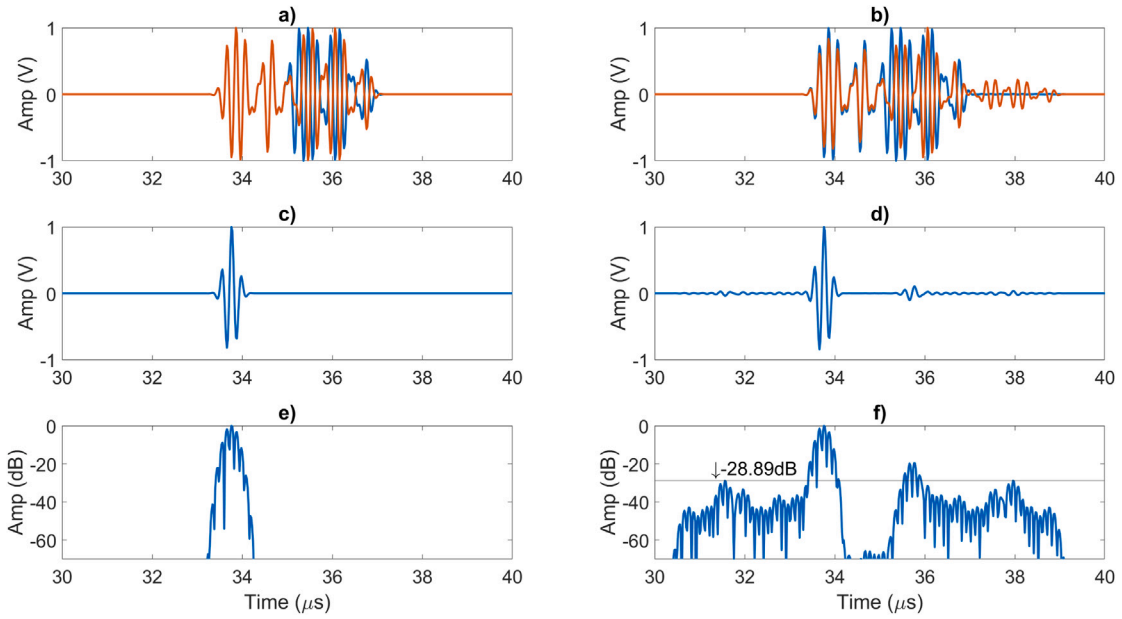


Fig. 16. Difference in appearance of simulated signals with and without 10 m/s sustained lateral motion across a 10 wavelength stepped defect in the front wall when using $L = 16$ CGS coded excitations with 1-cycle 5 MHz square wave symbols. *(a–b)* Corresponding echoes simulated using the CGS coded excitation signals and the simulation methodology outlined in Figs. 10 and 14. *(c–d)* Filtered output from the recorded signals in *a–b*. *(e–f)* Filtered output from the recorded signals in *a–b* shown on a log scale with the position and amplitude of the peak value in the SL measurement region indicated.

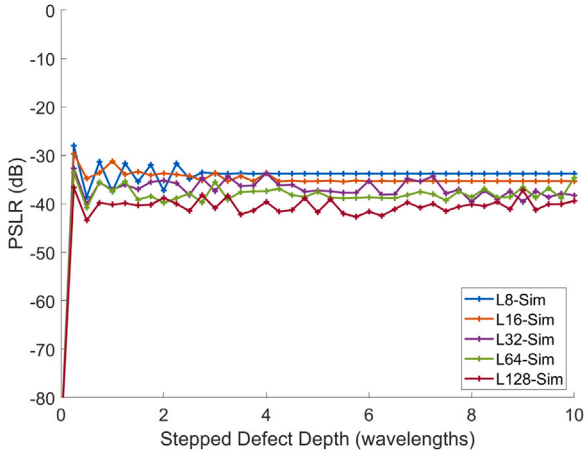


Fig. 17. Degradation in PSLR as stepped defect size increases when using CGS based coded excitations of increasing sequence length on a platform undergoing 5 m/s sustained lateral motion. A 1-cycle 5 MHz square wave symbol used for all measurements. Results obtained using the simulation methodology outlined in Figs. 10 and 14.

degradation. With lateral motion, symbol misalignment is minimal and the energy asymmetry between symbols is the predominant mechanism through which degradation occurs. As mentioned in Section 4, when energy asymmetry occurs, a longer sequence helps to reduce degradation severity by reducing the PSLR starting point, thus longer sequences are beneficial in lateral motion scenarios, up to a point (a longer excitation can inherently allow for a greater intra-sequence variation as total travel duration increases).

So far, only 2D simulation results for lateral motion have been presented. This is because the impact of introduced SLs would have been too small to notice given the simulations predict a PSLR less than our experimental noise floor. The C-scan tank that was used for the experiments to test the effect of motion towards a target has a maximum speed of 100 mm/s. Based on the simulated results, this would introduce artifacts 60 dB below the ML. These artifacts would not be seen given this C-scan experimental platform has a baseline SNR of approximately 40 dB (depending on sequence length and reflector surface). Nonetheless, the C-scan tank was used to record signals with sustained lateral motion of 100 mm/s to verify performance degradation did not occur. CGS based coded excitations ($L = 32$) were used with a 1-cycle 5 MHz square wave symbol and a mild steel reflector containing a stepped front wall defect was placed under the transducer face (a step of 3 mm taking the front wall surface from 20 mm to 23 mm from the transducer face). A collection of signals recorded from this setup are shown in Fig. 18.

The signals shown in Fig. 18 were taken as the transducer progressed across the stepped defect — starting from one material thickness in plot *(a)* and finishing at the second thickness in *(e)*. As the signals progress, it is clear to see the second ML corresponding to the stepped change in material thickness appear. The increasing amplitude of the second ML, and conversely decreasing amplitude of the initial ML, demonstrates the progression as more of the defect is covered by the transducer illuminated area. Despite the sustained motion of the transducer throughout the change in material thickness, no measurable PSLR degradation is observed, as was predicted by the simulations for such a low lateral motion velocity.

Overall, the simulations shown here indicate that lateral motion can introduce PSLR performance degradation, but only at substantial sustained motion velocities. The lack of capability to experimentally introduce degradation from lateral motion is of itself validation that coded excitation is robust against this degradation mechanism. The following section utilises an industrial application to verify that a beneficial outcome arises from the use of coded excitation when lateral motion is present.

5.3. Industrial application - RMS-600

The previous sections investigated the impact of motion towards and across reflectors on coded excitation compression performance in simulations and laboratory conditions. This section further shows results from implementing varying length coded excitations in a real world scanning application.

The real-world application used was a corrosion mapping tool from Eddyfi Technologies. The chosen platform utilised an RMS-600 raster

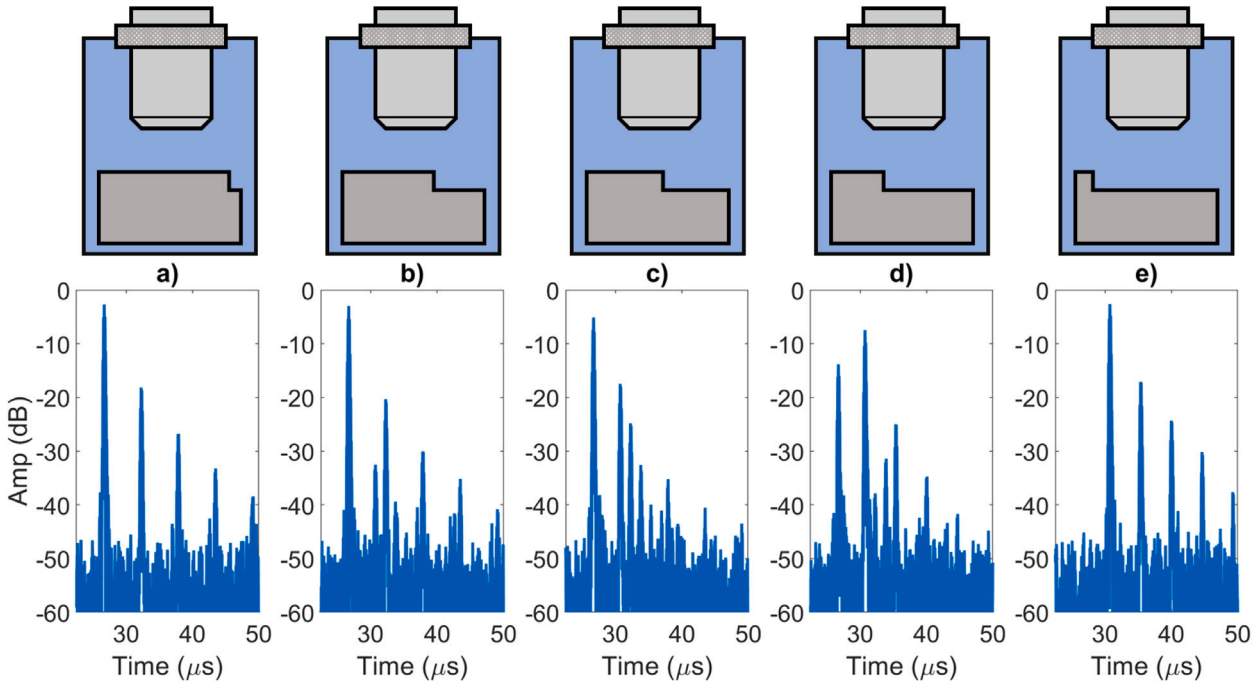


Fig. 18. Signals recorded using the C-scan experimental platform with $L = 32$ CGS coded excitations (1-cycle 5 MHz square wave symbol). The C-scan was set to laterally move the transducer at 100 mm/s across the surface of a reflector containing a 3 mm front wall stepped defect. Plots (a)–(e) show the signals as the transducer crossed the stepped defect.

scanning tool to laterally move a transducer (5 MHz, Krautkramer, 1 inch diameter, focused) over a fixed reflector. The RMS-600 motor stage facilitated lateral motion at a maximum speed of 730 mm/s and used a pumped water column (28 mm nominal coupling distance) to couple the transducer to the reflector. The reflector was set as 12.5 mm thick mild steel with a 3 mm stepped defect in the back wall — a pumped water column coupling did not allow for front wall defects to be captured.

The use of a pumped water column in this experimental setup allows for inconsistencies in couplant conditions to occur via the presence of air-bubbles and flow turbulence. Whilst couplant inconsistencies do not physically alter the distance between the transducer surface and the front wall of the reflector, they do change the propagation characteristics throughout the couplant. This is similar to the introduction of vertical motion as couplant propagation time can change on a symbol to symbol basis. Therefore, this experimental platform experiences both lateral and (equivalent to) vertical motion throughout the measurements making it an ideal candidate for testing the robustness of coded excitation.

The transducer placed in the RMS-600 was connected to the same acquisition electronics from previous experiments — an HS5 AFG and oscilloscope. This was used to record 500 measurements as the RMS-600 moved the transducer back-and-forth across the reflector. This process was undertaken for a standard uncoded measurement (a single 5 MHz bipolar square wave) as well as repeated for measurements using coded excitation of varying sequence lengths and types (all with 5 MHz square wave symbols). The results from using this platform are shown in Figs. 19–21.

Firstly, Fig. 19 shows a collection of the recorded signals when a standard excitation is used. The raw recorded signals are shown on a linear scale and the matched filtered signals are shown on a log scale. This figure gives an indication of the baseline signal quality achieved with this experimental setup. Firstly, all signals can be seen to contain high intensity pulses of coherent noise — this noise arises from interference with the motor drivers and it is not suppressed well by the matched filter. Fig. 19-(a) and (f) show signals when the transducer is above a non-defective material section, 19-(c) and (h) then shows the response when the transducer is crossing the stepped defect threshold, and 19-(d) and (i) shows signals within the defective region. In each of these signals, there is sufficient information pertaining to the back wall that either material thickness or simply the presence of a defect could be identified. In 19-(b), (g), (e) and (j), the signals were recorded whilst an inconsistency in the couplant conditions occurred — this has led to a significant reduction in either front or back wall echo SNR and has further introduced spurious artifact echoes.

Fig. 20 then shows a similar collection of signals which were recorded by using $L = 32$ CGS-based coded excitations. In these signals, there has been a notable increase in SNR, of the order approx. 15–20 dB, which is most visible when comparing the noise contained near the 35 μs region. This gain matches what is to be expected given the chosen CGS sequence length, and is further evidenced by the clear reduction in the level of coherent noise from the motor interference — the high frequency spikes are heavily suppressed. The signal recorded whilst the transducer is illuminating the defect stepped edge also contains no significant PSLR degradation around the back wall echoes, as expected for just 730 mm/s lateral motion. However, 20-(b), (g), (e) and (j) then show measurements taken whilst a couplant inconsistency event occurred. In these signals, there is clear PSLR performance degradation for the front wall echo — see the SLs present between 32-35 μs. This can be identified as a front wall compression error given the raw signals show differences in echo energy (and position) for each of the complementary pair. With uncoded measurements, such couplant variations result in very poor quality signals. With coded excitations, the signal quality remains higher, albeit with the addition of the unwanted filter artifacts arising from imperfect compression.

The signals shown in Figs. 19 and 20 can be used to draw initial conclusions. Firstly, coded excitation is robust in the face of lateral motion as even 730 mm/s movement across a significant stepped defect does not produce measurable PSLR degradation above the noise floor. Secondly, just like with conventional excitations, coded excitation is sensitive to couplant variations which can lead to a PSLR degradation. To demonstrate that an overall net benefit remains from using coded excitation, Fig. 21 shows the distribution in PSLR – measured as the front wall peak relative to the peak in the region immediately preceding

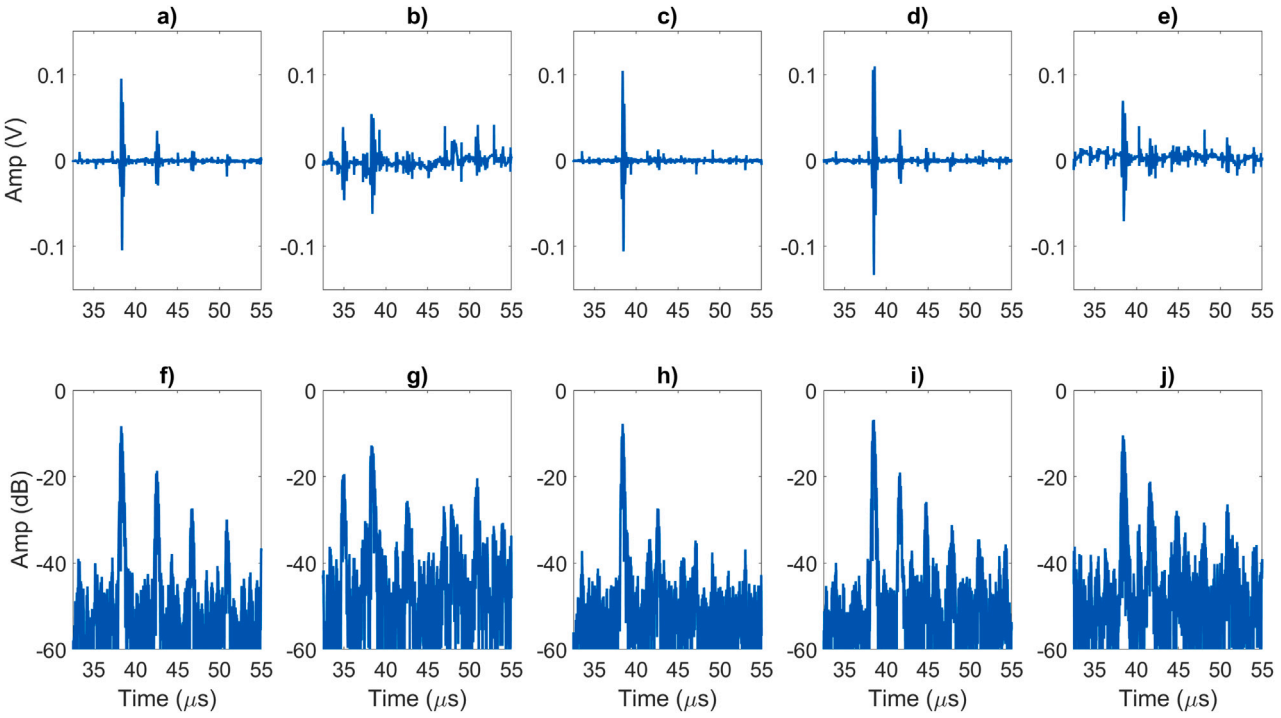


Fig. 19. Signals recorded on the RMS-600 experimental platform when using standard excitations (1-cycle 5 MHz bipolar square wave). First row shows raw recorded signals, second row shows the matched filtered signals on a log scale normalised to the maximum front wall echo amplitude across all measurements. Column 1 shows signals with the nominal reflector thickness. Columns 3 and 4 then show signals as the transducer traverses the stepped back wall defect. Columns 2 and 5 show signals over the nominal and defective thickness whilst a couplant variation event occurred.

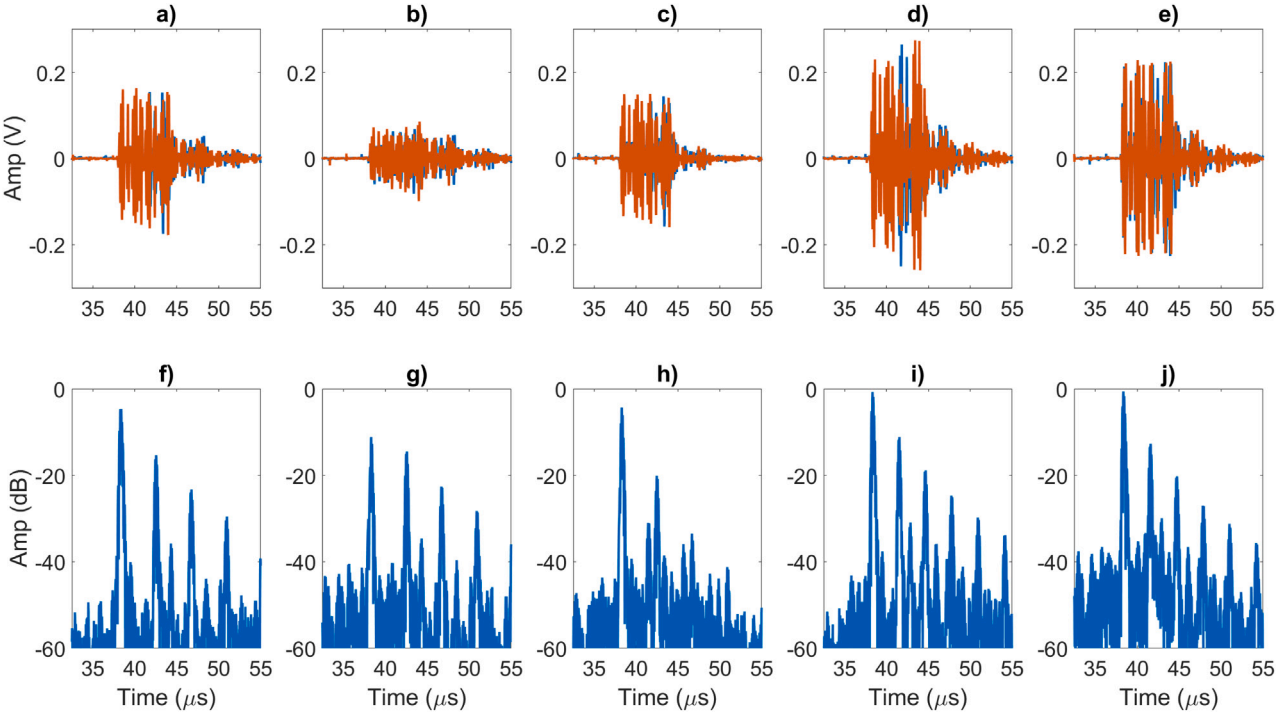


Fig. 20. Signals recorded on the RMS-600 experimental platform when using $L = 32$ CGS based coded excitations with a 1-cycle 5 MHz square wave symbol. First row shows raw recorded signals, second row shows the matched filtered signals on a log scale normalised to the maximum front wall echo amplitude across all measurements. Column 1 shows signals with the nominal reflector thickness. Columns 3 and 4 then show signals as the transducer traverses the stepped back wall defect. Columns 2 and 5 show signals over the nominal and defective thickness whilst a couplant variation event occurred.

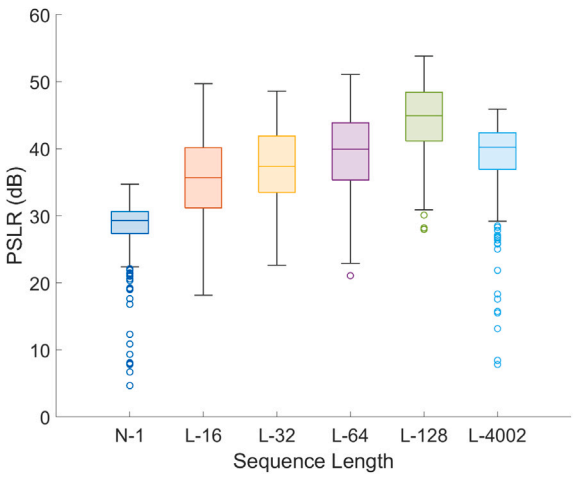


Fig. 21. Box-plots showing the PSLR (or worst-case SNR) distribution when using varying excitation signals on the RMS-600 experimental platform. $N-1$ references a standard uncoded measurement. $L-16$ to $L-128$ were CGS based coded excitations. $L-4002$ was a TOP-CS based coded excitation.

the front wall – across all 500 repeat measurements for varying coded excitation sequence lengths (and the standard excitation measurement).

From Fig. 21, uncoded measurements are shown to have a narrow range, but an overall low PSLR and there are many outlier signals with a very poor PSLR (from signals impacted by couplant variations and motor interference). Coded excitations with increasing length CGSs then have a wider range in signal quality but an overall higher median PSLR and less low quality outliers — this is explained by couplant variations resulting in a reduced PSLR in these conditions but most symbols are symmetric enough that a high quality ML is still produced. TOP-CS coded excitations were then used to produce the final box-plot which shows a high signal quality (despite using a low-power architecture) but with an increased number of low quality outliers given the extended transmission duration allows for a greater risk of couplant variation.

5.4. Discussion of measurement results in non-stationary scenarios

Overall, the results obtained from using the industrial scanning application, in combination with the previously presented simulation and experimental results for isolated vertical and lateral motion, show that coded excitation is an effective technique for improving signal quality and is sufficiently robust against symbol misalignment from realistic motion scenarios. Whilst the technique can suffer from PSLR performance degradation, the signals produced outperform a measurement from an equivalent industrial scenario (in terms of lateral or vertical motion) where a standard excitation signal was used by 6–15 dB on average.

6. Conclusions

In this work, we have investigated how robust coded excitation is when faced with imperfections in acquisition equipment and changes in measurement conditions. As part of this, we have described two main degradation mechanisms: Symbol Asymmetry and Symbol Misalignment. These degradation mechanisms reduce signal quality by introducing and re-positioning filter artifacts which can greatly increase the complexity for onward signal analysis. To track the performance degradation that can be introduced by these mechanisms, we used the maximum Peak-to-Side Lobe Ratio (PSLR) as a key metric to evaluate the quality of arising coded excitation signals when faced with both mechanisms.

The effect of symbol asymmetry degradation due to the presence of hardware imperfections was investigated using simulations and experiments. This focused on imbalances and asymmetries in the transmission electronics, such as DC offsets and unequal slew rates. From this, it was found that only a rail specific slew rate asymmetry had a substantial effect on PSLR. With just a 6 ns difference in rise or fall characteristics across the voltage rails, filter artifacts in excess of the measurement noise floor (40 dB below the ML peak) were introduced. System designers should therefore look to use hardware architectures that facilitate similar switching characteristics for positive and negative signals to avoid this issue, and should further use multi-cycle symbols and longer sequences to minimise hardware-induced asymmetry degradation. With a 2-cycle square wave symbol and CGSs of $L = 16$, a transmission architecture that has rise and fall times across rails within 10 ns of each other is required to ensure PSLR performance degradation does not exceed 40 dB.

The second major degradation mechanism, symbol misalignment, can occur when using coded excitations on non-stationary systems where movement between the transducer and the target introduces signal distortions. This was investigated both in simulation and experiment and it was shown that symbol misalignment can lead to significant performance degradation (artifacts ≥40 dB); however, this requires sustained motion of the transducer towards or away from a reflector at velocities ≥500 mm/s. This degradation can be minimised by using shorter sequences with shorter symbols (lower total excitation duration). Furthermore, during motion across a reflector, performance degradation does not occur unless there is a change in propagation characteristics, such as due to the presence of a defect in the measured material. In this scenario, our investigations showed that only minor performance degradation occurred even when considering relatively high velocities. It took ≥10 m/s sustained lateral motion across a 10 wavelength stepped wall loss defect to introduce ≥35 dB filter artifacts when using $L = 128$ CGSs. With lateral motion, longer sequences are instead preferred to reduce PSLR degradation.

Finally, we have used an industrial application with an RMS-600 corrosion mapping tool to demonstrate the net benefits achieved when using coded excitation when system motion occurs. The signals recorded on this platform using coded excitation were of a higher quality compared to uncoded measurements despite 730 mm/s of lateral motion and changes in couplant conditions due to the use of a pumped water column. Net gains in signal quality from using coded excitation (SNR improvements in excess of 15 dB with traditional CGSs) were achieved in these imperfect operating conditions.

Overall, this work has shown that coded excitations are susceptible to a performance degradation when faced with imperfections in measurement conditions. However, the technique is mostly robust against both symbol asymmetry and symbol misalignment and can be used to achieve net beneficial improvements once symmetry conditions are understood.

CRediT authorship contribution statement

Connor Challinor: Writing – original draft, Methodology, Investigation, Formal analysis, Conceptualization. **Frederic Cegla:** Writing – review & editing, Supervision, Methodology, Funding acquisition, Formal analysis.

Declaration of competing interest

The authors declare the following financial interests/personal relationships which may be considered as potential competing interests: Connor Challinor reports financial support was provided by NDT Global. Connor Challinor has patent #GB2304842.4 pending to Imperial College Innovations Limited. Frederic Cegla has patent #GB2304842.4 pending to Imperial College Innovations Limited. If there are other authors, they declare that they have no known competing financial interests or personal relationships that could have appeared to influence the work reported in this paper.

Acknowledgements

The authors would like to acknowledge funding from NDT Global and the EPSRC via the FIND CDT (EP/S023275/1). Furthermore, we would like to thank Antonio De-Sanctis for his technical support in the laboratory. Finally, we would like to thank former and current supporters at NDT Global – Jochen Giese and Michael Haas – and Eddyfi Technologies – Neil Pearson – for their assistance in project supervision and useful discussions, and Thierry Couturier at Eddyfi Technologies for reviewing this work.

Data availability

Data will be made available on request.

References

[1] P. Burrascano, S. Callegari, A. Montisci, M. Ricci, M. Versaci, M. Tucci, Ultrasonic Nondestructive Evaluation Systems: Industrial Application Issues, Springer Science+Business Media, New York, New York, 2015-2015.

[2] T. Misaridis, J. Jensen, Use of modulated excitation signals in medical ultrasound. part i: basic concepts and expected benefits, IEEE Trans. Ultrason. Ferroelectr. Freq. Control 52 (2) (2005) 177–191, http://dx.doi.org/10.1109/TUFFC.2005.1406545.

[3] R. Chiao, X. Hao, Coded excitation for diagnostic ultrasound: a system developer's perspective, IEEE Trans. Ultrason. Ferroelectr. Freq. Control 52 (2) (2005) 160–170, http://dx.doi.org/10.1109/TUFFC.2005.1406543.

[4] D. Hutchins, P. Burrascano, L. Davis, S. Laureti, M. Ricci, Coded waveforms for optimised air-coupled ultrasonic nondestructive evaluation, Ultrason. 54 (7) (2014) 1745–1759, http://dx.doi.org/10.1016/j.ultras.2014.03.007.

[5] T. Kaddoura, R.J. Zemp, Hadamard aperiodic interval codes for parallel-transmission 2D and 3D synthetic aperture ultrasound imaging, Appl. Sci. 12 (10) (2022) http://dx.doi.org/10.3390/app12104917.

[6] E.P. Vienneau, B.C. Byram, A coded excitation framework for high SNR transcranial ultrasound imaging, IEEE Trans. Med. Imaging (2023) http://dx.doi.org/10.1109/TMI.2023.3269022, 1–1.

[7] E. Vienneau, B. Byram, Compound barker-coded excitation for increased signal-to-noise ratio and penetration depth in transcranial ultrasound imaging, in: 2020 IEEE International Ultrasonics Symposium, IUS, 2020, pp. 1–4, http://dx.doi.org/10.1109/IUS46767.2020.9251650.

[8] D. Lines, E. Mohseni, Y. Javadi, C. Mineo, R. Vithanage, Z. Qiu, C. MacLeod, G. Pierce, A. Gachagan, Using coded excitation to maintain signal to noise for FMC+TFM on attenuating materials, in: 2019 IEEE International Ultrasonics Symposium, IUS, 2019, pp. 635–638, http://dx.doi.org/10.1109/ULTSYM.2019.8925564.

[9] R. Challis, V. Ivchenko, R. Al-Lashi, Ultrasonic attenuation measurements at very high SNR: Correlation, information theory and performance, J. Phys.: Conf. Ser. 457 (2013) http://dx.doi.org/10.1088/1742-6596/457/1/012004.

[10] M. Ricci, L. Senni, P. Burrascano, Exploiting pseudorandom sequences to enhance noise immunity for air-coupled ultrasonic nondestructive testing, IEEE Trans. Instrum. Meas. 61 (11) (2012) 2905–2915, http://dx.doi.org/10.1109/TIM.2012.2200409.

[11] J. Isla, F. Cegla, Coded excitation for pulse-echo systems, IEEE Trans. Ultrason. Ferroelectr. Freq. Control 64 (4) (2017) 736–748, http://dx.doi.org/10.1109/TUFFC.2017.2661383.

[12] J.A. Isla, F.B. Cegla, Simultaneous transmission and reception on all elements of an array: Binary code excitation, Proc. R. Soc. A: Math. Phys. Eng. Sci. 475 (2019) http://dx.doi.org/10.1098/rspa.2018.0831.

[13] M. Tamraoui, H. Liebgott, E. Roux, Complete complementary coded excitation scheme for snr improvement of 2d sparse array ultrasound imaging, IEEE Trans. Biomed. Eng. (2023) 1–14, http://dx.doi.org/10.1109/TBME.2023.3325657.

[14] E. García, J.A. Paredes, F.J. Álvarez, M.C. Pérez, J.J. García, Spreading sequences in active sensing: A review, Signal Process. 106 (2015) 88–105, http://dx.doi.org/10.1016/j.sigpro.2014.07.002.

[15] D. Sarwate, M. Pursley, Crosscorrelation properties of pseudorandom and related sequences, Proc. IEEE 68 (5) (1980) 593–619.

[16] M. Yang, C. Chakrabarti, Design of orthogonal coded excitation for synthetic aperture imaging in ultrasound systems, in: 2012 IEEE International Symposium on Circuits and Systems, ISCAS, 2012, pp. 113–116, http://dx.doi.org/10.1109/ISCAS.2012.6271430.

[17] C. Challinor, N. Pearson, F. Cegla, Coded excitation using TOP-CS sequences for multi-channel low-power ultrasonics, Mech. Syst. Signal Process. 213 (2024) 111339, http://dx.doi.org/10.1016/j.ymssp.2024.111339.

[18] C. Challinor, F. Cegla, Pulse compression with and without matched filtering: Why codes beat chirps, NDT E Int. 147 (2024) 103180, http://dx.doi.org/10.1016/j.ndteint.2024.103180.

[19] T. Misaridis, J. Jensen, Use of modulated excitation signals in medical ultrasound. part ii: design and performance for medical imaging applications, IEEE Trans. Ultrason. Ferroelectr. Freq. Control 52 (2) (2005) 192–207, http://dx.doi.org/10.1109/TUFFC.2005.1406546.

[20] T. Misaridis, J. Jensen, Use of modulated excitation signals in medical ultrasound. part iii: high frame rate imaging, IEEE Trans. Ultrason. Ferroelectr. Freq. Control 52 (2) (2005) 208–219, http://dx.doi.org/10.1109/TUFFC.2005.1406547.

[21] G. Turin, An introduction to matched filters, IRE Trans. Inf. Theory 6 (3) (1960) 311–329, http://dx.doi.org/10.1109/TIT.1960.1057571.

[22] M. Golay, Sieves for low autocorrelation binary sequences, IEEE Trans. Inform. Theory 23 (1) (1977) 43–51, http://dx.doi.org/10.1109/TIT.1977.1055653.

[23] M. Golay, Complementary series, IRE Trans. Inf. Theory 7 (2) (1961) 82–87, http://dx.doi.org/10.1109/TIT.1961.1057620.

[24] F. Fiedler, J. Jedwab, M.G. Parker, A framework for the construction of golay sequences, 2006.

[25] M.G. Parker, K.G. Paterson, C. Tellambura, Golay complementary sequences, in: Wiley Encyclopedia of Telecommunications, John Wiley & Sons, Ltd, 2003, http://dx.doi.org/10.1002/0471219282.eot367.

[26] Maxim Integrated, Max14808/max14809 – octal three-level/quad five-level high-voltage 2a digital pulsers with t/r switch, 2024, https://www.analog.com/en/products/max14808.html. product page - (Accessed 19 August 2024).

[27] STMicroelectronics, Sthv800 – octal /-90 v, /-2 a, 3-level rtz, high-speed ultrasound pulser, 2024, https://www.st.com/en/switches-and-multiplexers/sthv800.html. product page - (Accessed 19 August 2024).

[28] TiePie Engineering, Handyscope HS5 USB oscilloscope with function generator, 2025, https://www.tiepie.com/en/usb-oscilloscope/handyscope-hs5#specifications product page - (Accessed 31 March 2025).

[29] J.H. Jobling, E.A. Saunders, T. Barden, M.J. Lowe, B. Lan, A feasibility study on phase characterisation of nickel-based superalloys using ultrasound, NDT E Int. 145 (2024) 103120, http://dx.doi.org/10.1016/j.ndteint.2024.103120.

[30] B. Lan, T. Ben Britton, T.-S. Jun, W. Gan, M. Hofmann, F.P. Dunne, M.J. Lowe, Direct volumetric measurement of crystallographic texture using acoustic waves, Acta Mater. 159 (2018) 384–394, http://dx.doi.org/10.1016/j.actamat.2018.08.037.